Gradient jump penalty stabilisation of spectral/hp element discretisation for under-resolved turbulence simulations

Rodrigo C. Moura[a], Andrea Cassinelli[b], André F. C. da Silva[a], Erik Burman[c], Spencer J. Sherwin[b,*]

[a]*Instituto Tecnológico de Aeronáutica, Brasil*
[b]*Imperial College London, UK*
[c]*University College London, UK*

Abstract

One of the strengths of the discontinuous Galerkin (DG) method has been its balance between accuracy and robustness, which stems from DG's intrinsic (upwind) dissipation being biased towards high frequencies/wavenumbers. This is particularly useful in high Reynolds-number flow simulations where limitations on mesh resolution typically lead to potentially unstable under-resolved scales. In continuous Galerkin (CG) discretisations, similar properties are achievable through the addition of artificial diffusion, such as spectral vanishing viscosity (SVV). The latter, although recognised as very useful in CG-based high-fidelity turbulence simulations, has been observed to be sub-optimal when compared to DG at intermediate polynomials orders ($P \approx 3$). In this paper we explore an alternative stabilisation approach by the introduction of a continuous interior penalty on the gradient discontinuity at elemental boundaries, which we refer to as a gradient jump penalisation (GJP). Analogous to DG methods, this introduces a penalisation at the elemental interfaces as opposed to the interior element stabilisation of SVV. Detailed eigenanalysis of the GJP approach shows its potential as equivalent (sometimes superior) to DG dissipation and hence superior to previous SVV approaches. Through eigenanalysis, a judicious choice of GJP's P-dependent scaling parameter is made and found to be consistent with previous a-priori error analysis. The favourable properties of the GJP stabilisation approach are also supported by turbulent flow simulations of the incompressible Navier-Stokes equation, as we achieve high-quality flow solutions at $P = 3$ using GJP, whereas SVV performs marginally worse at $P = 5$ with twice as many degrees of freedom in total.

Keywords: high-order discretisation, spectral/hp element method, stabilised methods, velocity splitting scheme, dispersion-diffusion analysis, temporal eigenanalysis, spatial eigenanalysis

---

*Corresponding author
Email address:* `s.sherwin@imperial.ac.uk` (Spencer J. Sherwin)

1. Introduction

The design of computational methods for complex flow problems at high Reynolds number remains an outstanding challenge in scientific computing. An approach that has received increasing interest recently is the implicit Large Eddy Simulation [1], or maybe more accurately termed, under-resolved Direct Numerical Simulation, where poorly resolved scales are regularised by the stabilising properties of the numerical scheme. The use of a stable numerical scheme ensures that the discrete solution can be computed, but in order for the solution to be fully reliable, all the scales of the flow must be resolved. In most practical cases, however, since only a finite range of scales can be resolved due to cost limitations, energy accumulating on the finest scales must be artificially dissipated.

The question is then which mechanism is best suited for the task of dissipating the energy. One natural choice in the context of high order methods is to use the polynomial modes for scale separation and let viscosity act on the highest polynomial modes only. This is the original idea behind the spectral viscosity method of Maday and Tadmor [2]. This approach acts as a low pass filtering, where one must choose the weights determining the strength of the viscous dissipation on different polynomial scales. It has been shown that for hyperbolic conservation laws an appropriate choice leads to convergence to entropy solutions [3, 4]. Although spectral viscosity methods have been extensively applied to turbulent flows, see e.g. [5], the downside of this approach is that the approximation power of the highest polynomial orders is sacrificed to ensure stability. As was shown in [6] a dispersion-diffusion (eigen)analysis may be used to tune the form of the spectral viscosity. This allows for the design of dissipation profiles (i.e. how dissipation is distributed) already in Fourier space.

An alternative strategy is to rely on upwind dissipation, naturally present in discontinuous spectral element methods (SEM) from interface fluxes. These provide the dissipative mechanism in a consistent fashion through the coupling condition of the convection term across solution discontinuities (jumps) between adjacent elements. The discontinuous Galerkin (DG) method is currently perhaps the most popular scheme amongst discontinuous SEM [7]. For linear model problems, DG's numerical stability comes from the convective term being contained in the finite element space up to a low order perturbation, whereas optimal accuracy is a consequence of DG's consistency and from the approximation properties of the (element-wise polynomial) spaces adopted [8]. The performance of DG for high Reynolds and turbulent flows has been studied in a number of works, see for instance [9, 10, 11, 12, 13]. DG's dissipation profile in Fourier space was particularly discussed in [12, 13], which highlighted the importance of its dissipation being biased towards high frequencies/wavenumbers, just as in spectral viscosity approaches. The latter, however, even in modern versions [14], still fall short in achieving the balance between accuracy and robustness that upwind DG offers. Many in the continuous SEM community, nevertheless, might find that DG has the disadvantages of higher implementation complexity due to the need to evaluate advective and diffusive interface terms (also for velocity-pressure coupling terms, in

most incompressible DG formulations), more degrees of freedom for the same approximation order and the need for bespoke solvers. It is natural, therefore, to ask the question as to whether continuous SEM might benefit from a stabilisation strategy similar to that of DG.

One might argue that DG introduces scale separation simply by relying on discontinuous elements such that unresolved energy concentrations are allowed to take place in the form of nonphysical jumps in the solution. With this view, it is natural to make dissipation act on interface jumps, which is exactly what upwind fluxes do. In the case of continuous SEM, the natural scale separation occurs between C^0 and C^1 continuity. One would expect nonphysical energy to concentrate as kinks in the solution at elemental interfaces, in which case the natural dissipative mechanism would then be a penalty on the jump of the normal gradient across element faces. This argument actually leads to the continuous interior penalty (CIP) method originally proposed by Douglas and Dupont in [15], which introduces a penalty on the jump of the gradient of the solution at elemental boundaries. This technique can be implemented by the addition of a specific term in the discrete formulation that, as shown in the present study, has indeed the effect of dissipating the high frequency content in the solution for turbulent flows. To stress this effect we will herein refer to the method as the Gradient Jump Penalty (GJP) stabilisation.

The improved stability of the CIP/GJP method was analysed by Burman and Hansbo for convection–diffusion in [16] and extended to the case of high Reynolds-number laminar solutions of the incompressible Navier-Stokes' equations in [17, 18]. It has indeed been shown that the same stability properties enjoyed by the DG method in the high order case carries over to the CG method with gradient jump penalty [19]. For a comparison of mathematical properties of the two interior penalty methods we refer to [20]; for a review of stabilised methods for high order methods for transport, see [21], and for a review of different stabilised methods for the incompressible Navier-Stokes' equations we refer to [22]. The CIP/GJP technique has several interesting features for large scale computations of the Navier-Stokes equations. No changes are required in the standard Galerkin part of the discretisation, with the stabilisation being symmetric and completely decoupled from the time discretisation. The same technique can be used for the stabilisation of both velocity-pressure coupling and convective instabilities, resulting in a method with considerable numerical stability for high Reynolds flows. The method does not need to be tuned to change scaling when the flow is resolved. A potential drawback is that the penalty on the gradient jump couples degrees of freedom of adjacent elements, further extending the stencil. However, since the stabilisation operator is symmetric, it is in general possible to treat it explicitly under a standard hyperbolic CFL condition [23]. Indeed, it is straightforward to integrate this method in standard fractional step pressure projection schemes to obtain an efficient solution method for the discrete scheme [24].

Although the method has been thoroughly analysed in the high Reynolds regime for the case of smooth (i.e. laminar) solutions, less work has been done in the turbulent case. For two-dimensional 'turbulent' solutions, there are some partial results. In [25] it was shown numerically that the stabilisation

decreases under refinement at a rate compatible with the power spectrum of the flow and, in [26], optimal error estimates independent of the Reynolds number and the solution regularity were derived under an assumption of scale separation of the solution in slow varying, energy carrying large eddies and strongly varying fine scale fluctuations with small energy. Recently, further computational work on two-dimensional problems in the high Reynolds regime has been carried out in [27, 28] with special focus on a comparison with computations using $H(div)$-conforming elements.

The objective of the present contribution is to study how the CIP-method / GJP-stabilisation behaves when applied as a stabilising mechanism for the spectral/hp continuous Galerkin (CG) method having in mind implicit LES / under-resolved DNS. In section 2, we show that the orthogonal projection of the convective term of the Navier-Stokes' equation on the complement in L^2 to the finite element space is indeed controlled by the gradient jump term. Contrary to the upwind term in the DG method, here the stabilisation term includes a parameter whose scaling is not known in principle. Values for this parameter have been discussed ever since the CIP method was first proposed, through numerical experimentation for low order elements and also via a priori error analysis which gives the asymptotic scaling for high polynomial orders [29]. Theoretical optimal values of the parameter for fixed polynomial orders have not been derived so far. To this end, in section 3 we consider the dispersion-diffusion (eigen)analysis of the GJP-stabilisation in a one-dimensional context. This leads to a judicious choice of the scaling parameter based on both temporal and spatial eigenanalyses. Finally, in section 4 we explore the behaviour of the gradient penalty term when applied to a linear advection problem and under-resolved simulations of turbulent flows in three dimensions.

2. Identifying under-resolved scales through orthogonal decomposition

In an under-resolved Galerkin approximation of incompressible flow it is well known that for high Reynolds numbers the high frequency energy is not dissipated at a high enough rate and it can therefore accumulate on the finest scales of the computational space. This high frequency energy build-up then generates oscillations that pollute under-resolved flows at high Reynolds number. The variational multi-scale approach to dissipating the scales provoking the energy build-up, is based on dissipating the scales of the convective term orthogonal to the finite element space [30]. Let V_h denote the finite element space of continuous functions consisting of piecewise polynomials of order P on each element. The convective term of the Galerkin discretisation of the incompressible Navier-Stokes' equations takes the form, for $u_h, v_h \in [V_h]^d$

$$c(u_h; u_h, v_h) := ((u_h \cdot \nabla)u_h, v_h)_\Omega = (\Pi_P(u_h \cdot \nabla)u_h, v_h)_\Omega$$

where $(\cdot, \cdot)_\Omega$ denotes $[L^2(\Omega)]^d$ scalar product, and $\Pi_P : [L^2(\Omega)]^d \mapsto [V_h]^d$ the L^2-projection. We see that the Galerkin approximation corresponds to projecting the convective terms on the scales of the

4

test space. However the Galerkin method is conservative and the energy of the orthogonal scales will remain, although invisible to the formulation. The fact that they are orthogonal to the test space makes them spurious and hence a good choice for the artificial dissipation. This is also the key idea behind the numerical analysis of (laminar) high Reynolds flow (see for instance [17, 30, 31, 24]). The question is then how to introduce dissipation corresponding to the orthogonal subscales in the computation. A natural choice was proposed by Codina in [32]

$$s(u_h, v_h) = (\tau h\, U^{-1}((u_h \cdot \nabla)u_h - \Pi_P(u_h \cdot \nabla)u_h), (u_h \cdot \nabla)v_h)_\Omega$$

where τ is a dimensionless parameter, h a mesh size and $U \in \mathbb{R}^+$ a characteristic speed which gives the term the right dimension. We also observe that

$$\|(\tau h\, U^{-1})^{\frac{1}{2}}((u_h \cdot \nabla)u_h - \Pi_P(u_h \cdot \nabla)u_h)\|_\Omega^2 = s(u_h, u_h).$$

Another dissipative mechanism that is more localised can be obtained by observing that the first singular scales of the finite element method are represented by the jump of the gradient over the faces of the mesh. This suggest that a penalty on the jump of the gradient over element faces should dissipate under-resolved scales while leaving resolved scales unpolluted of artificial dissipation. In particular for high order elements there is a non-trivial C^1 subspace that evolves in the kernel of the stabilisation. However considering a monodomain discretisation it is clear also that the gradient jump term can not dissipate all the scales. We will therefore show below how the the orthogonal subscales can be controlled by one term penalising the jump of the gradient and another that dissipates high frequency energy inside the element due to the product of two poynomials.

Let $\{\mathcal{T}\}_h$ denote a family of tesselations, $\mathcal{T} := \{\Omega^e\}$, indexed by h representing the mesh parameter defined as the largest diameter of any element $\Omega^e \in \mathcal{T}$. We will denote the set of interior faces of $\mathcal{T}$ by $\mathcal{F}$. To each face we associate a fixed normal n_F. We will use the following norm on the mesh skeleton

$$\|v\|_\mathcal{F} = \left(\sum_{F \in \mathcal{F}} \|v\|_F^2\right)^{\frac{1}{2}}.$$

We introduce the space of functions that are polynomials on each element

$$X_h := \{x \in L^2(\Omega) \text{ such that } x|_{\Omega^e} \in \mathbb{P}_P(\Omega^e), \forall \Omega^e \in \mathcal{T}\}.$$

We let $\pi_P : [L^2(\Omega)]^d \mapsto [X_h]^d$ denote the vector valued L^2-projection on $[X_h]^d$. The jump of a discontinuous quantity, $\xi_h \in X_h$ over an interior face F (i.e. a face not in the domain boundary) will be denoted

$$[\![\xi_h]\!]|_F := \lim_{\epsilon \to 0^+} \xi_h(x - n_F\epsilon) - \xi_h(x + n_F\epsilon), \quad x \in F.$$

The following approximation result for discrete spaces was proved in [19].

Lemma 1. *Let $v_h \in X_h$ then there holds*

$$\inf_{w_h \in V_h} \|v_h - w_h\|_\Omega \leq c \| \left(\frac{h}{P}\right)^{\frac{1}{2}} [\![v_h]\!] \|_{\mathcal{F}}.$$

It follows that we can bound the quantity that we want to dissipate by jumps over element faces in the following fashion:

$$\inf_{w_h \in [V_h]^d} \|((u_h \cdot \nabla)u_h - w_h\|_\Omega$$

$$= \inf_{w_h \in [V_h]^d} \|((1-\pi_P)(u_h \cdot \nabla)u_h + \pi_P(u_h \cdot \nabla)u_h - w_h\|_\Omega$$

$$\leq \|((1-\pi_P)(u_h \cdot \nabla)u_h\|_\Omega + \inf_{w_h \in [V_h]^d} \|\pi_P(u_h \cdot \nabla)u_h - w_h\|_\Omega$$

$$\leq \|((1-\pi_P)(u_h \cdot \nabla)u_h\|_\Omega + c\| \left(\frac{h}{P}\right)^{\frac{1}{2}} [\![\pi_P(u_h \cdot \nabla)u_h]\!] \|_{\mathcal{F}}. \qquad (1)$$

To obtain an upper bound using the jump of the gradient we add and subtract $(u_h \cdot \nabla)u_h$ in the jump of the right hand side and proceed using the triangle inequality followed by a trace inequality [33] to obtain

$$\|[\![\pi_P(u_h \cdot \nabla)u_h]\!]\|_{\mathcal{F}} \leq \|[\![(1-\pi_P)(u_h \cdot \nabla)u_h]\!]\|_{\mathcal{F}} + \|[\![(u_h \cdot \nabla)u_h]\!]\|_{\mathcal{F}}$$

$$\leq c\|Ph^{-\frac{1}{2}}((1-\pi_P)(u_h \cdot \nabla)u_h\|_\Omega + c\|[\![(u_h \cdot \nabla)u_h]\!]\|_{\mathcal{F}}.$$

We have proved the following result

Proposition 1. *There exists $C > 0$, independent of h and P such that for all $u_h \in [V_h]^d$ there holds*

$$\inf_{w_h \in [V_h]^d} \|((u_h \cdot \nabla)u_h - w_h\|_\Omega \leq C(P^{\frac{1}{2}}\|((1-\pi_P)(u_h \cdot \nabla)u_h\|_\Omega + \|(hP^{-1})^{\frac{1}{2}}[\![(u_h \cdot \nabla)u_h]\!]\|_{\mathcal{F}}).$$

In order to write a stabilisation that is based on a sum over the elements we introduce the average of the flux over a face F such that $F = \partial\Omega_1^e \cap \partial\Omega_2^e$ as

$$\mathcal{G}(u_h)|_F := \nabla u_h|_{\partial\Omega_1^e \cap F} \cdot n_1 + \nabla u_h|_{\partial\Omega_2^e \cap F} \cdot n_2 \qquad (2)$$

where n_i, $i = 1, 2$ denotes the outward pointing normal of element Ω_i^e and $\nabla u_h|_{\partial\Omega^e} := \lim_{\epsilon \to 0^+} \nabla u_h(x - \epsilon n_{\Omega^e})$ for $x \in \partial\Omega^e$. Proposition 1 and the *hp*-analysis for convection-diffusion equations of [19] suggests the following stabilisation term on isotropic discretisations, here the continuity of the approximation space has been used to simplify the contribution from the jumps:

$$s(u_h, v_h) = (\tau_0 h(|u_h| + U_0)^{-1}(1-\pi_P)(u_h \cdot \nabla)u_h, (u_h \cdot \nabla)v_h)_\Omega + \left\langle \tau_1|u_h \cdot n|h_{\Omega^e}^2 \mathcal{G}(u_h)\frac{\partial v_h}{\partial n} \right\rangle \qquad (3)$$

In equation (3) the angle brackets denote integration over the trace of the element, i.e.

$$\left\langle \ \right\rangle = \sum_{T \in \Omega^e} \int_{\partial\Omega^e \setminus \partial\Omega} ds$$

6

and n denotes the outward normal of the elements Ω^e. Observe that the stabilisation term has been split into two terms, one that is completely local to each element, similar to a spectral viscosity and one that acts on fluctuations over element boundaries. If a discontinuous Galerkin method with conservative fluxes is considered a similar form is obtained, with the only difference that in that case the jump of the solution itself is penalised over element boundaries. The dimensionless parameters τ_0 and τ_1 depend on the mesh geometry and the polynomial order. Below we will only consider the second term. In [19] the scaling $\tau_1 = P^{-3.5}$ was proposed based on a hp-a priori error analysis. However in the following we adopt a scaling of $\tau_1 \propto (P+1)^{-4}$ motivated by the eigen-analysis in the next section.

The form (3) is then added as a weakly consistent numerical viscosity to the discrete Navier-Stokes' model. More precisely if we let the forms $a(v, w)$, $b(v, q)$, $c(x; w, v)$ denote the viscous, pressure and convective term respectively of the Navier-Stokes equations the semi-discretisation in space takes the form: find $(u_h, p_h) \in [V_h]^d \times Q_h$ such that

$$(\partial_t u_h, v_h)_\Omega + c(u_h; u_h, v_h) + b(v_h, p_h) + b(u_h, q_h) + a(u_h, v_h) + s(u_h, v_h) = 0 \tag{4}$$

for all $(v_h, q_h) \in [V_h]^d \times Q_h$. If the velocity pair $[V_h]^d \times Q_h$ does not satisfy the inf-sup condition a term similar to (3) but acting on the pressure can be added to ensure pressure stability [31]. The fact that the stabilisation term is independent from the equations makes it straightforward to apply (and analyse) efficient time stepping approaches such as fractional step pressure projection methods [24] or implicit-explicit time-stepping [34]. For instance the nonlinear term together with stabilisation $c + s$ can be treated explicitly under certain CFL conditions, also in the high Reynolds regime, thus mitigating the additional costs of nonlinear solves and the extended matrix stencil introduced by (3).

3. Temporal and spatial 1D eigenanalyses

In this section we consider an eigenanalysis of the gradient jump penalty stabilisation introduced in the previous section to verify the scaling in P of the stabilisation parameter τ_1. For the sake of simplicity, we will henceforward refer to this parameter as just τ. This analysis is motivated by previous works [35, 36, 37, 38] where the GJP stabilisation was developed and further highlights its potential as a high-order stabilisation approach for the incompressible Navier–Stokes equations.

In these previous works the focus was on a priori error estimates for smooth solutions. However in the following the objective is to assess how the diffusion introduced by GJP stabilisation is distributed in spectral (wavenumber or frequency) space. We will demonstrate through the analysis that GJP introduces diffusion in a way that is superior to what has been achieved so far with spectral vanishing viscosity (SVV) [39, 14]. More specifically, GJP is found capable of yielding diffusion levels similar to those of (standard upwind) DG at the same polynomial order without featuring non-monotonic oscillations in the dispersion curves. Nevertheless, these benefits are only obtained for a relatively

narrow range of the GJP penalty parameter. Fortunately, the eigen-analysis can easily determine this range which is consistent for both the spatial and temporal analysis considered and also agrees with the asymptotic relation obtained for the dependence on the polynomial order of the penalty parameter obtained through a-priori error analysis.

3.1. Discrete Matrix Formulation

We consider the linear advection–diffusion equation in one dimension, namely

$$\frac{\partial u}{\partial t} + a\frac{\partial u}{\partial x} = \mu\frac{\partial^2 u}{\partial x^2} , \tag{5}$$

where a is the advection speed and μ is the viscosity coefficient. The spectral/hp element discretisation within an elemental interval

$$\Omega_e = \{x_e \le x(\xi) \le x_{e+1}; -1 \le \xi \le 1\} \text{ and } h = x_{e+1} - x_e$$

is of the form, (cf. Eq. (7) in Ref. [39]),

$$\int_{\Omega_e} \phi_i \frac{\partial u}{\partial t} \, dx + a\int_{\Omega_e} \phi_i \frac{\partial u}{\partial x} \, dx + \mu\int_{\Omega_e} \frac{\partial \phi_i}{\partial x}\frac{\partial u}{\partial x} \, dx = 0 , \tag{6}$$

where ϕ_i denotes an element-wise polynomial basis function from the set $\hat{\phi} = \{\phi_1, \ldots, \phi_{P+1}\}^T$.

Recalling the form (3), the GJP stabilisation consists of adding a right-hand side term to Eq. (6) of the form

$$-\tau\,|a|\,h^2\left\langle\frac{\partial \phi_i}{\partial n}\,\mathcal{G}\right\rangle , \tag{7}$$

where we recall that τ is the penalty parameter, h is the grid size (assumed constant) and $\mathcal{G}$ (introduced in equation (2)) is the numerical gradient-jump and n denotes the outward normal of the elements. Obviously for a one-dimensional element the trace is just a point evaluation at the ends of the segment. If we denote by $\ominus$ and $\oplus$ the left and right interfaces of Ω_e respectively, we can define

$$\left\langle\frac{\partial \phi_i}{\partial n}\,\mathcal{G}\right\rangle = \left.\frac{\partial \phi_i}{\partial x}\right|_{\oplus} n_{\oplus}\,\mathcal{G}_{\oplus}^e + \left.\frac{\partial \phi_i}{\partial x}\right|_{\ominus} n_{\ominus}\,\mathcal{G}_{\ominus}^e , \tag{8}$$

where $(\partial\phi/\partial x)_{\oplus}$ and $(\partial\phi/\partial x)_{\ominus}$ represent the basis evaluated at the left and right elemental interface, and similarly $n_{\oplus}, n_{\ominus}$ are the normals at the left and right interfaces and so $n_{\oplus} = 1$ and $n_{\ominus} = -1$. Further, $\mathcal{G}_{\oplus}$ denotes the gradient-jump at the interface between Ω_e and the adjacent element Ω_{e+1}, so that

$$\mathcal{G}_{\oplus}^e = \left.\frac{\partial u}{\partial n}\right|_{\oplus}^e + \left.\frac{\partial u}{\partial n}\right|_{\ominus}^{e+1} = \left.\frac{\partial u}{\partial x}\right|_{\oplus}^e - \left.\frac{\partial u}{\partial x}\right|_{\ominus}^{e+1} = \frac{2}{h}\left[\left.\frac{\partial u}{\partial \xi}\right|_1^e - \left.\frac{\partial u}{\partial \xi}\right|_{-1}^{e+1}\right] .$$

where we have assumed an affine mapping between the standard region $-1 \le \xi \le 1$ and the elemental interval $\Omega_e = \{x_e < x < x_{e+1}\}$ which leads to the constant geometric factor $\frac{\partial \xi}{\partial x} = 2/h$. Analogously, $\mathcal{G}_{\ominus}^e$ denotes the gradient-jump at the interface between Ω_e and the adjacent element Ω_{e-1}

$$\mathcal{G}_{\ominus}^e = \left.\frac{\partial u}{\partial n}\right|_{\ominus}^e + \left.\frac{\partial u}{\partial n}\right|_{\oplus}^{e-1} = -\left.\frac{\partial u}{\partial x}\right|_{\oplus}^e + \left.\frac{\partial u}{\partial x}\right|_{\ominus}^{e-1} = -\frac{2}{h}\left[\left.\frac{\partial u}{\partial \xi}\right|_{-1}^e - \left.\frac{\partial u}{\partial \xi}\right|_1^{e-1}\right] .$$

Denoting the vector of element-wise solution coefficients within Ω_e as $\hat{u}^e = \{u_1, \ldots, u_{P+1}\}_e^T$ and that of the basis functions' derivatives as $\hat{\phi}' = \{\phi_1', \ldots, \phi_{P+1}'\}$, with $\phi_i' = \partial \phi_i / \partial \xi$, leads to

$$\mathcal{G}_\oplus = \frac{2}{h} \left[\hat{\phi}_\oplus' \, \hat{u}^e - \hat{\phi}_\ominus' \, \hat{u}^{e+1} \right], \quad \mathcal{G}_\ominus = -\frac{2}{h} \left[\hat{\phi}_\ominus' \, \hat{u}^e - \hat{\phi}_\oplus' \, \hat{u}^{e-1} \right].$$

We can now write expression (8) in terms of the local derivatives with respect to ξ as

$$\left\langle \frac{\partial \phi_i}{\partial n} \mathcal{G} \right\rangle = \frac{4}{h^2} \left[(\phi_i')_\oplus^T \left[\hat{\phi}_\oplus' \, \hat{u}^e - \hat{\phi}_\ominus' \, \hat{u}^{e+1} \right] + (\phi_i')_\ominus^T \left[\hat{\phi}_\ominus' \, \hat{u}^e - \hat{\phi}_\oplus' \, \hat{u}^{e-1} \right] \right].$$

Finally we have obtained a matrix evaluation of the GJP operator (3.1) in the form

$$\left\langle \frac{\partial \hat{\phi}}{\partial n} \mathcal{G} \right\rangle = \frac{4}{h^2} \left[-\Delta_\ominus^\oplus \, \hat{u}_{e+1} + \Delta_\oplus^\oplus \, \hat{u}_e + \Delta_\ominus^\ominus \, \hat{u}_e - \Delta_\oplus^\ominus \, \hat{u}_{e-1} \right], \tag{9}$$

where the matrices introduced above are defined as

$$\Delta_\ominus^\oplus = (\hat{\phi}')_\oplus^T (\hat{\phi}')_\ominus, \quad \Delta_\oplus^\oplus = (\hat{\phi}')_\oplus^T (\hat{\phi}')_\oplus,$$

$$\Delta_\ominus^\ominus = (\hat{\phi}')_\ominus^T (\hat{\phi}')_\ominus, \quad \Delta_\oplus^\ominus = (\hat{\phi}')_\ominus^T (\hat{\phi}')_\oplus. \tag{10}$$

In summary, using (9) and (7) the following matrix form is obtained for the semi-discrete linear advection–diffusion equation with added GJP terms and $a > 0$ (cf. Eq. (11) in Ref. [39]):

$$\frac{h}{2a} \mathbf{M} \frac{\partial \hat{u}_e}{\partial t} + \mathbf{A} \, \hat{u}_e + \frac{2}{\text{Pe}} \mathbf{D} \, \hat{u}_e = 4\tau \left[\Delta_\ominus^\oplus \, \hat{u}_{e+1} - \left(\Delta_\oplus^\oplus + \Delta_\ominus^\ominus \right) \hat{u}_e + \Delta_\oplus^\ominus \, \hat{u}_{e-1} \right], \tag{11}$$

where $\text{Pe} = ah/\mu$ and

$$\mathbf{M}[i,j] = \int_{-1}^{1} \phi_i \phi_i \, d\xi, \quad \mathbf{A}[i,j] = \int_{-1}^{1} \phi_i \phi_j' \, d\xi, \quad \mathbf{D}[i,j] = \int_{-1}^{1} \phi_i' \phi_j' \, d\xi. \tag{12}$$

For the case $\tau = 0$ we obviously recover the traditional advection–diffusion discretisation which is transformed into a global problem through an assembly process [40]. The global assembly process when $\tau = 0$ would only couple three elements as is the case in [39]. However when $\tau \neq 0$ the structure of (11) will couple five elements through the global assembly process due to the GJP stabilisation terms.

Independently of how many elements are coupled through global assembly, one can decouple from the global system to a series of blocks related to the restricted set of element-wise coefficients $\hat{c}_j = \{u_1, \ldots, u_P\}_j^T$, in which the last entry is not absorbed into the first element through the assembly process (see [39] for further details), for which one can write

$$\frac{h}{2a} \left(\mathcal{L}_\mathbf{M} \frac{\partial \hat{c}_{e-1}}{\partial t} + \mathcal{C}_\mathbf{M} \frac{\partial \hat{c}_e}{\partial t} + \mathcal{R}_\mathbf{M} \frac{\partial \hat{c}_{e+1}}{\partial t} \right) = \mathcal{L}_\mathbf{X} \, \hat{c}_{e-1} + \mathcal{C}_\mathbf{X} \, \hat{c}_e + \mathcal{R}_\mathbf{X} \, \hat{c}_{e+1} +$$

$$+ \mathcal{L}_\mathbf{\Delta}' \, \hat{c}_{e-2} + \mathcal{L}_\mathbf{\Delta} \, \hat{c}_{e-1} + \mathcal{C}_\mathbf{\Delta} \, \hat{c}_e + \mathcal{R}_\mathbf{\Delta} \, \hat{c}_{e+1} + \mathcal{R}_\mathbf{\Delta}' \, \hat{c}_{e+2}, \tag{13}$$

where (13) above recovers Eq. (17) of Ref. [39], in which the matrices with subscript $\mathbf{X}$ stem from both advection and diffusion terms while the matrices with subscript $\mathbf{\Delta}$ above stem from the GJP terms on the right-hand side of (11).

To proceed with the eigen-analysis, one assumes

$$\hat{c}_j \ \propto \ \hat{\zeta} \ \exp\left[i(\kappa x_j - \omega t)\right] \ , \tag{14}$$

so that $\hat{c}_{j\pm 1} = \exp(\pm i\kappa h)\,\hat{c}_j$ and $\hat{c}_{j\pm 2} = \exp(\pm 2i\kappa h)\,\hat{c}_j$. Inserting these into (13) leads to an eigenvalue problem of size P, namely

$$-i\varpi h\hat{\zeta} = \mathbf{Z}_P\hat{\zeta} \ , \tag{15}$$

in which $\varpi = \omega/a$ and $\mathbf{Z}_P = \mathbf{Z}_P(\kappa h, \mathrm{Pe}, \tau)$ is our $P \times P$ eigenmatrix, given by

$$\mathbf{Z}_P = 2\left[\mathcal{L}_{\mathbf{M}}\,z^{-1} + \mathcal{C}_{\mathbf{M}} + \mathcal{R}_{\mathbf{M}}\,z\right]^{-1}\left[\mathcal{L}'_{\mathbf{\Delta}}\,z^{-2} + \mathcal{L}_{\mathbf{X\Delta}}\,z^{-1} + \mathcal{C}_{\mathbf{X\Delta}} + \mathcal{R}_{\mathbf{X\Delta}}\,z + \mathcal{R}'_{\mathbf{\Delta}}\,z^2\right] \ , \tag{16}$$

where $\mathcal{L}_{\mathbf{X\Delta}} = \mathcal{L}_{\mathbf{X}} + \mathcal{L}_{\mathbf{\Delta}}$, $\mathcal{C}_{\mathbf{X\Delta}} = \mathcal{C}_{\mathbf{X}} + \mathcal{C}_{\mathbf{\Delta}}$, $\mathcal{R}_{\mathbf{X\Delta}} = \mathcal{R}_{\mathbf{X}} + \mathcal{R}_{\mathbf{\Delta}}$ and $z = \exp(i\kappa h)$.

Given Pe and τ, a set of P values for ϖh can be obtained as the complex-valued eigenvalues of (15) for each chosen (real) value of κh. Through this approach we obtain the eigencurves of the temporal analysis. In the spatial analysis, an equivalent determinant problem is considered, namely,

$$\det\left[\mathbf{Z}_P(\kappa h) + i\varpi h\mathbf{I}_P\right] = 0 \ , \tag{17}$$

where $\mathbf{I}_P$ is the identity matrix of size P. In this approach, given Pe and τ, for each real value of ϖh, one has to numerically obtain all the possible (complex) values of $z = \exp(i\kappa h)$ for which (17) is true. Typically, only two roots exist, one representing a physical mode and another corresponding to a spurious reflected mode [41, 14]. Interestingly, when considering GJP stabilisation, four roots are found. These are covered in Sec. 3.3, whereas the temporal analysis is discussed first, in the next section.

3.2. Temporal eigenanalysis

The temporal analysis approach assumes periodic boundary conditions and therefore the related results are particularly important for computations with one or more directions along which numerical periodicity is adopted. Plots of numerical dispersion and diffusion are obtained through the eigenvalues of equation (15). More specifically, for each real-valued $\kappa\hbar$, one finds P complex-valued $\varpi\hbar$, whose real and imaginary parts represent dispersion and diffusion, respectively. Amongst the corresponding P eigencurves, one can identify the so-called primary curves [42, 39], which recover the unique dispersion and diffusion behaviour rather than the P-valued series of curves. Only primary eigencurves are considered here. Note that s $\kappa\hbar$ and $\varpi\hbar$ are typically used to quantify under-resolution since $\hbar = h/P$ represents the "mesh size" of a single numerical DOF [42, 39, 43].

In order to assess GJP diffusion, the limit of very large Péclet is considered, such that viscous diffusion effects are negligible. This scenario is specially relevant to high-Reynolds turbulent flow simulation since at each polynomial order, the only parameter to be adjusted is τ. As first highlighted in [39], continuous Galerkin (CG) projections may exhibit potentially undesirable features at either very large or very small
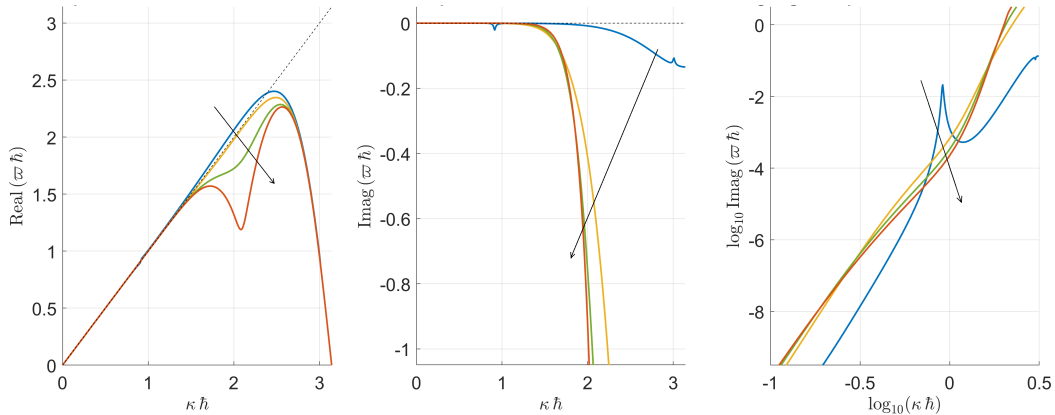
Figure 1: Numerical dispersion (left) and diffusion (middle) curves for $P = 3$ with values of τ increasing from 1×10^{-4} through to 1.5×10^{-2}, as indicated by the arrow. The diffusion curves are also shown on a log-log scale on the right.

Péclet numbers due to non-smooth or non-monotonic eigencurves. This has also been noted in [44] in the context of under-resolved turbulence simulations with HDG methods. In fact, SVV operators have been specially designed in [14] to guarantee monotonic diffusion profiles in Fourier space. These, however, yielded for P-th order CG the diffusion levels of DG at order $P - 2$, which is sub-optimal since ideally a diffusion level of order P would be observed. For the GJP method on the other hand, when τ is chosen within the "well behaved" range mentioned above, GJP diffusion levels for P-th order CG are found to be between those of (standard upwind) DG of orders P and $P + 1$. This is a notable benefit in terms of accuracy and demonstrates considerable potential for GJP stabilisation.

For example, when considering $P = 3$, the range of τ where non-oscillatory eigencurves are found is approximately $7 \times 10^{-4} < \tau < 1.1 \times 10^{-2}$. A slightly wider range is covered in Fig. 1, where τ values are shown from 1×10^{-4} until 1.5×10^{-2}. Oscillatory dispersion and/or diffusion profiles are clearly seen at these limits. In particular for the case when $\tau = 1 \times 10^{-4}$ we observe two diffusion spikes in the middle plot, one of which is more clearly observed in log-log scale shown in the right-most plot.

The appropriate range of τ becomes narrower as P is increased, and a representative value for τ within this range has been chosen for each P. The corresponding eigencurves are shown for $P = 1$ to $P = 3$ in Figs. 2 and for $P = 4$ to $P = 9$ in Appendix A. These plots show that monotonic diffusion curves are in fact yielded by appropriate values of τ (indicated in the plots), that spectral resolution power (on a per-DOF basis) increases consistently as P grows, and that diffusion levels of P-th order CG stay between those of (standard upwind) DG of order P and $P + 1$. The reference DG diffusion lines shown in the right-most plots follow the asymptotic levels of DG's superconvergence and are approximated through a simple formula [45], namely

$$\log_{10}(\varpi_i \hbar) \approx 2(P + 1)\log_{10}(\kappa \hbar) - (P + 1)/2 \, , \tag{18}$$

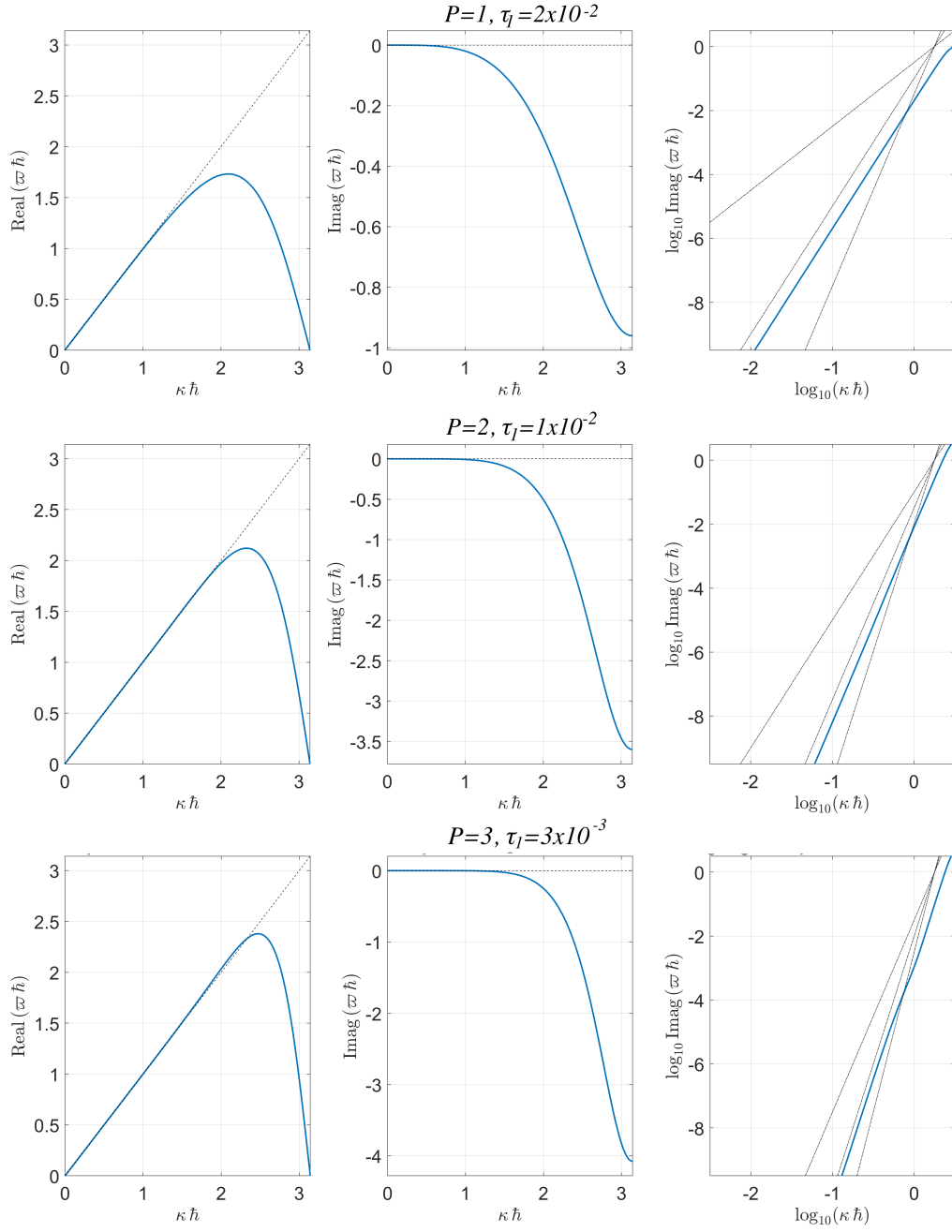where ϖ_i denotes the absolute value of $\text{Imag}(\varpi)$.

Figure 2: Numerical dispersion (left) and diffusion (middle) curves for $P = 1, \tau = 2 \times 10^{-2}$ (top), $P = 2, \tau = 1 \times 10^{-2}$ (middle) and $P = 3, \tau = 1 \times 10^{-3}$ (bottom) with well behaved values of τ for each order. The diffusion curves are also shown in log-log scale on the right, where diffusion levels of (standard upwind) DG at orders $P - 1$, P and $P + 1$ are included by the increasing slope of the thin dash-dotted lines for reference.

3.3. Spatial eigenanalysis

The so-called spatial analysis approach assumes inflow/outflow-type boundary conditions and is arguably more relevant to practical simulations, despite the fact that temporal analyses (that assume periodic conditions) are more often found in the literature. The results yielded by spatial analysis concern the evolution of waves in a numerical solution that originate after an incoming wave of given frequency ω hits an interface between two elements or an outflow boundary. In general, some waves are transmitted and some are reflected, all of them preserving the same frequency of the incoming wave. Having in mind the exact solution of the PDE under consideration, it is clear that only one of these waves is physical, which should be a transmitted wave. In the case of linear advection, the exact behaviour of this transmitted wave is well known, i.e. it should have wavenumber $\kappa = \omega/a = \varpi$ and zero diffusion. Numerical error changes this behaviour depending on the level of under-resolution. When $\varpi \hbar \to 0$, the exact behaviour should be recovered.

The waves featured in spatial analyses have a real-valued frequency ω and a complex-valued wavenumber κ, whose real and imaginary parts define respectively their dispersive and diffusive behaviour. By denoting $\mathrm{Real}(\kappa) = \kappa_r$ and $\mathrm{Imag}(\kappa) = \kappa_i$, one can write

$$u \propto \exp[-\kappa_i x] \exp\{i[\kappa_r x - \omega t]\} \ . \tag{19}$$

This shows that, in a stable scheme, transmitted waves must have $\kappa_i > 0$ such that they decay while moving forwards ($\Delta x > 0$), whereas reflected waves must have $\kappa_i < 0$ in order to decay while moving backwards ($\Delta x < 0$). This topic is discussed in more detail in [14]. In the GJP study considered here, four complex-valued κ have been found for each real-valued ϖ. These comprise two transmitted and two reflected waves. All of them, except the physical transmitted wave, have been found to be strongly damped (numerically dissipated) given appropriate values for the penalty parameter τ. The four solutions to problem (17) have been obtained algebraically via Matlab's symbolic manipulation functionalities. This methodology has been motivated by a previous study [46] on DG's spatial analysis, and is considered more robust than root-finding algorithms used in previous works [41, 14].

We consider, once more, the limit of large Péclet numbers so that viscous diffusion effects are negligible and only GJP-based diffusion is relevant, so that τ is the only parameter to be varied in the analysis for each given polynomial order. Fortunately, the range of τ for which smooth spatial eigencurves (including monotonic diffusion curves) has been found to be consistent with those observed in the temporal analysis. In addition, the GJP diffusion levels found within this "well behaved" range for each order P have also been found to be in between those of (same-DOF standard upwind) DG of orders P and $P + 1$. This not only leads to a consistent increase in resolution power as P grows [42, 47], but also indicates that temporal and spatial analysis seem to go hand-in-hand for GJP stabilisation. This was not the case with SVV, for example, where smooth kernel functions are suggested as ideal by temporal analysis
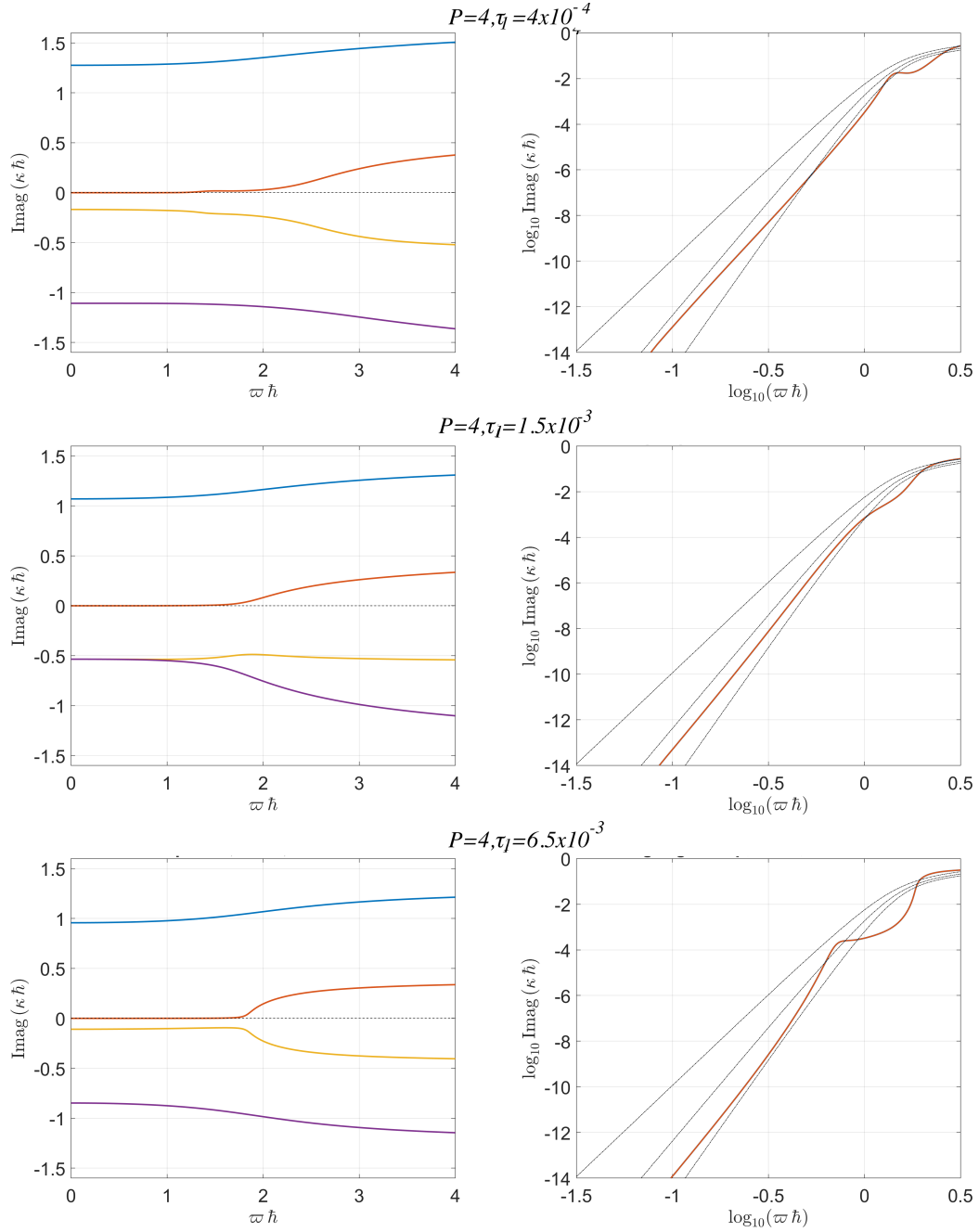
13

Figure 3: GJP diffusion eigencurves for $P = 4$ of all four waves (left) and of the physical wave alone in log-log scale (right) as the penalty parameter is increased from $\tau = 4 \times 10^{-4}$ (top) to $\tau = 1.5 \times 10^{-3}$ (middle) until $\tau = 6.5 \times 10^{-3}$ (bottom). In each sub-plot on the left the two upper curves are transmitted waves, whereas the two lower curves are reflected waves. The diffusion curves of (standard upwind) DG at orders $P-1$, P and $P+1$ are included as dash-dotted lines on the log-log plots for reference.
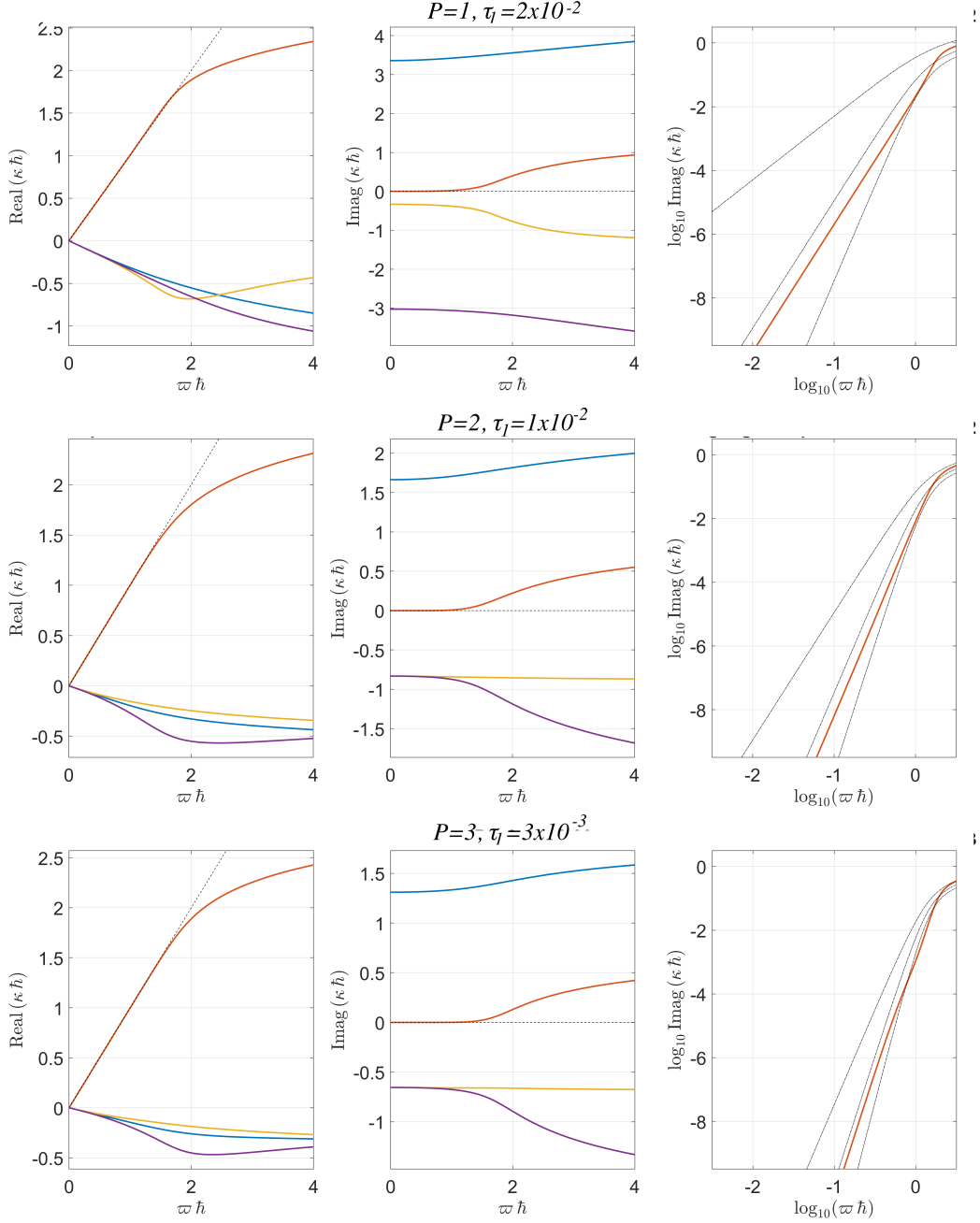
Figure 4: Numerical dispersion (left) and diffusion (middle) curves for $P = 1, \tau = 2 \times 10^{-2}$(top) $P = 2, \tau = 1.8 \times 10^{-2}$ and $P = 3, \tau = 3 \times 10^{-3}$ (bottom). The diffusion curve of the physical mode (red) is also shown in log-log scale on the right, where reference curves of (standard upwind) DG at orders $P - 1$, P and $P + 1$ are included as dash-dotted lines.

[39], whereas non-smooth ones are motivated by spatial analysis [14]. As a result, in the subsequent discussion, the same values of $\tau = \tau(P)$ chosen in the temporal analysis of the previous section will be used here in the spatial analysis' plots.

Before showing the complete plots for each order, however, it is useful to discuss the typical behaviour of spatial eigencurves when τ values outside the well behaved range are chosen. This is demonstrated for $P = 4$ in Fig. 3, where the penalty parameter is increased from $\tau = 4 \times 10^{-4}$ until $\tau = 6.5 \times 10^{-3}$. Plots on the left show diffusion curves for all the four waves mentioned previously, whereas the corresponding log-log plots on the right display only the physical wave's diffusion (using the same red colour), along with reference DG diffusion curves at orders $P - 1$, P and $P + 1$. As suggested by the top-right graph, τ values smaller than 4×10^{-4} featured non-smooth diffusion profiles. On the other hand, τ values larger than 6.5×10^{-3}, while not yet featuring non-monotonic diffusion for the physical mode, lead to small diffusion levels for a reflected mode (yellow curve) as $\mathrm{Imag}(\kappa\hbar)$ becomes close to zero. Ideally, all spurious waves should have $|\mathrm{Imag}(\kappa\hbar)| > 0.1$, which is a reference value for moderate diffusion proposed in [14].

Note that as τ is increased within the range under consideration for $P = 4$, the spurious reflected mode is initially more damped, then reaches a level of maximum diffusion and finally becomes less damped, moving towards negligible diffusion levels if τ is further increased. Spurious waves should be strongly damped, as they can otherwise lead to accuracy loss and possibly numerical instability [43, 14] while interacting with the physical part of the numerical solution. These two aspects, namely, monotonic diffusion for the physical mode and sufficient diffusion of spurious ones, are the basic criteria adopted here when defining well behaved ranges for τ. As already mentioned, these have been found to be somewhat similar to those found in the context of temporal analysis, whereby the same values of τ chosen in Sec. 3.2 have been adopted here. The corresponding spatial eigencurves (now including dispersion plots) for $P = 1$ to $P = 3$ are shown in Figs. 4 and for $P = 4$ to $P = 9$ in appendix Appendix A. The log-log graphs in these figures, in particular, closely resemble those shown in Sec. 3.2 for the temporal analysis.

It is finally worth noting that the adopted values of $\tau = \tau(P)$, although chosen by visual inspection of the curves, appear to match the values suggested by the a-priori error analysis of [19]. In the latter case "optimal" τ values scale as $\tau = \alpha P^{-3.5}$. In Fig. 5 we present a comparison of the experimental (denoted by symbols) and theoretical values of τ, using the $\tau = 0.28(P + 1)^{-3.5}$ and $\tau = 0.8(P + 1)^{-4}$. We observe that the first fit, shown in figure 5(a), spans the whole interval from $1 \leq P \leq 9$ reasonably well. We can however achieve a slightly better fit in the interval $2 \leq P \leq 9$ using the fit shown in figure 5 (b) but have to make a special case for $P = 1$ when $\tau = 0.02$. In the following section we will adopt this second fit for the choice of τ. Nevertheless, the conclusion is that the a-priori error analysis and the dispersion analysis both suggest very similar optimal values of τ.
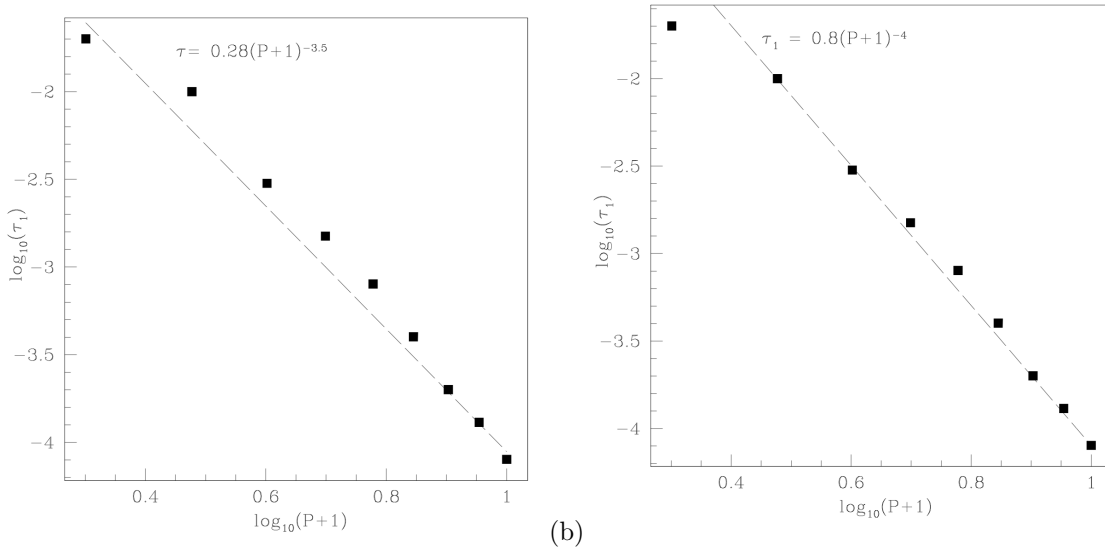
Figure 5: Comparison between the scaling (a) $\tau = 0.28(P+1)^{-3.5}$ and (b) $\tau = 0.8(P+1)^{-4}$ and the optimal experimental values obtained shown by square symbols.

3.4. Eigenanalysis Summary

One of the insights provided by eigenanalysis concerns the distribution of diffusion in spectral (wavenumber of frequency) space. This topic has been investigated both in the context of temporal and spatial analyses, which assume either periodic or inflow/outflow-type boundary conditions, respectively. This study has highlighted that when a penalty parameter τ is chosen within a certain range, the GJP stabilisation does not suffer from non-smooth dispersion/diffusion features that might affect simulation quality for under-resolved computations. Values of τ for polynomial orders $P = 1$ to $P = 9$ have been obtained that ensure smoothly-varying diffusion profiles in spectral space, as well as sufficiently strong diffusion of spurious eigenmodes/waves. The latter have been found in previous studies [43, 41, 14] to directly impact solution accuracy and numerical stability unless strongly dissipated.

A notable benefit of GJP, however, when compared to previously developed stabilisation techniques suited for the simulation of (possibly under-resolved) transitional and turbulent flows, is that it introduces small diffusion levels while providing sufficient stability/robustness. For example, the best balance achieved previously in [14] between accuracy and robustness for spectral vanishing viscosity (SVV) stabilising CG of order P required diffusion levels similar to those of (standard upwind) discontinuous Galerkin (DG) schemes of order $P-2$. With GJP diffusion levels between those of DG of orders P and $P+1$ are typically obtained. This highlights the potential of GJP for CG-based high-fidelity simulations of transitional and turbulent flows, including implicit LES or under-resolved DNS approaches. However this analysis is only for idealised equally spaced one-dimensional problems and has not considered non-modal temporal analysis [44] which might also be relevant. More realistic tests are required to determine

17

the benefits of GJP over alternative stabilisation techniques which will be considered in section 4.

4. Results

In the following we consider the addition of the GJP stabilisation as an explicit contribution to the time dependent simulation of both a scalar linear advection equation and the incompressible Navier-Stokes equations. The explicit addition of GJP stabilisation (7) is added to the right hand side of the weak form of the equation as shown in equation (6) for the advection-diffusion problem. Finally we also require the definition of the three parameters τ_1, a and h which are evaluated as:

- For τ_1 we use the fit to the experimental data for well-behaved eigencurves, namely:

$$\tau_1 = \begin{cases} 0.02 & P = 1 \\ 0.8(P+1)^{-4} & P > 1 \end{cases}$$

- The explicit implementation of the stabilisation allows for both a fixed or dynamics evaluation of the characteristic velocity a. In the following we have adopted a fixed $a = 1$ value in the scalar advection equation. However for the more complex meshes adopted in the incompressible Navier-Stokes simulation we have evaluated $a(s)$ along an edge or face as absolute value of the normal velocity over the edge or face.

- The characteristic element size h is estimated in the following manner. For each vertex that lies on an edge or face we identify the out-of-plane edge that does not lie within the edge or face or interest. This out-of-plane edge is attached to a unique out-of-plane vertex and we determine the perpendicular length from this out-of-plane vertex to the local edge or face. We then evaluate the average of these perpendicular distances and use it as the choice of h along the edge or face within each element.

4.1. Linear advection equation

To illustrate the effect of the GJP stabilisation we consider its influence on the solution to the linear advection equation

$$\frac{\partial \phi}{\partial t} + \mathbf{U} \cdot \nabla \phi = 0. \tag{20}$$

The linear advection equation is explicitly evaluated using a continuous Galerkin spectral/hp element discretisation. The discretisation was advanced using a classical fourth order Runge Kutta scheme and as mentioned above the GJP stabilisation term is explicitly added to weak form of the Galerkin discretisation.
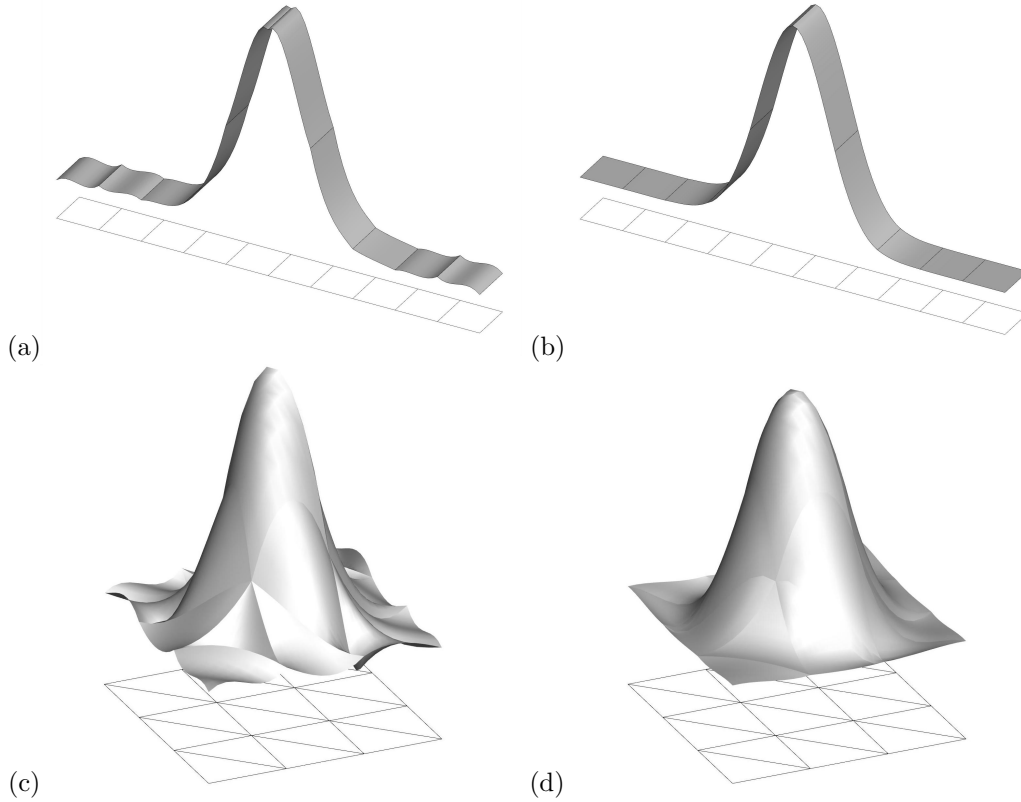
(a)

(b)

(c)

(d)

Figure 6: Advection in quadrilateral and triangular domains at $P = 3$.

In figure 6(a) and (b) we show the solution of the advection problem (20) on a linear set of ten square domains of size 0.2 over the region $0 - 1 < x < 1, 0 < y < 0.2$ with an advection velocity of $\mathbf{U} = [1, 0]^T$ and an initial condition of

$$\phi(x, y) = \exp(-20x^2)$$

Using a time step of $\Delta t = 0.01$ and a polynomial order of $P = 3$, figure 6(a) shows the solution at $T = 2$ after one periodic propagation through the domain. In contrast figure 6 (b) shows the same problem with the Gradient Jump Penalty stabilisation where it is clear the oscillation between the elemental boundaries have been significantly reduced.

Figures 6(c) and (d) shows an analogous two-dimensional problem over a quadrilateral domain consisting of 18 triangular elements of similar shape and covering the region $0 < x, y < 1$. In this case the advection velocity was $\mathbf{U} = [1, 1]^T$ and the initial condition was

$$\phi(x, y) = \exp(-20((x - 0.5)^2 + (y - 0.5)^2))$$

Using a time step of $\Delta t = 0.001$ and a polynomial order of $P = 3$, figure 6(c) shows the solution at

$T = 1$ after one diagonal propagation through the periodic domain. Finally figure 6 (d) shows the same problem with the Gradient Jump Penalty stabilisation where it is again clear the oscillation between elemental boundaries have been significantly reduced.

4.2. Incompressible flow past a circular cylinder at $Re = 3900$

To provide a more quantive analysis on a more challenging problem we next apply the GJP stabilisation in the context of the flow past a circular cylinder. This is a popular benchmarking problem which features a wide variety of flow phenomena, and as such it has traditionally been a reference test case to validate the accuracy and performance of numerical solvers.

The wake dynamics is strongly dependent on the Reynolds number [48]. The present study focuses on the subcritical regime at $Re = 3900$. At this Reynolds number, the flow in the vicinity of the cylinder is entirely laminar, and transition occurs in the separated shear layers leading to a fully turbulent wake. The GJP stabilisation presented in this study is compared with the a DG-Kernel approach for Spectral Vanishing Viscosity (SVV) stabilisation [14], here referred to as DGK, which has been applied to a range of industrial flow problems [49, 50].

4.2.1. Computational approach

The incompressible Navier-Stokes equations

$$\frac{\partial \mathbf{u}}{\partial t} = -(\mathbf{u} \cdot \nabla)\mathbf{u} - \nabla p + \nu \nabla^2 \mathbf{u} \qquad \text{in } \Omega\,, \qquad (21a)$$

$$\nabla \cdot \mathbf{u} = 0 \qquad \text{in } \Omega\,, \qquad (21b)$$

were discretised using the spectral/hp element framework *Nektar++* [51]. Time advancement follows the stiffly stable time discretisation proposed by Karniadakis et al. [52], also known as Velocity-Correction Scheme [53]. As part of this formulation, the convective terms are treated explicitly, while pressure and the viscous contributions are treated implicitly, thus circumventing stability constraints associated with the viscous time stepping. All simulations also rely on the use of spectral/hp dealiasing for consistent integration of the nonlinear terms, based on the work by Mengaldo et al. [54]. The curved boundaries are handled with an isoparametric mapping, so that the curvature is defined using at least a subset of the basis functions used to represent the solution field [55]. Moreover, the implementation adopted in the present work relies on Taylor-Hood type elements, where the C^0 continuous pressure field is computed at one polynomial order lower than the C^0 continuous velocity variables. The nature of the problem allows to combine a spectral element discretization in the $x - y$ planes with with a Fourier expansion in the spanwise homogeneous direction. When applied to the incompressible flow equations, this approach is considerably more efficient than a fully three-dimensional implementation, since linear operators can be Fourier-transformed into a series of two-dimensional operators. The implicit equations were solved using

20

an efficient direct solver with multi-level static condensation [55]. Stabilisation in the Fourier direction is obtained by means of SVV, which introduces an additional operator defined as:

$$S_{vv} = \mu_{SVV} \frac{\partial}{\partial x} \left(\hat{Q} \star \frac{\partial u}{\partial x} \right), \tag{22}$$

where μ_{SVV} is a constant coefficient, $\star$ denotes the convolution operator and $\hat{Q}$ is the kernel that regulates which modes receive how much damping. For this homogeneous direction, an exponential kernel is adopted [56]:

$$\hat{Q}_k = \begin{cases} \exp \left(-\frac{(k-N)^2}{(k-P_{\text{cut}})^2} \right), & k > P_{\text{cut}}, \\ 0, & k \leq P_{\text{cut}}, \end{cases} \tag{23}$$

with $\mu_{SVV} = 1$ and $P_{\text{cut}} = 0.5N$, with N indicating the number of modes. The stabilisation in the $x-y$ planes is obtained by means of DG-Kernel approach for SVV (DGK) or GJP.

The computational geometry adopted for all simulations is shown in Figure 7a. A uniform inflow velocity $\mathbf{u} = [1, 0, 0]^T U_\infty$ was prescribed, and no-slip conditions were imposed on the cylinder boundary. Free-stream boundary conditions were adopted for the top and bottom portions of the domain. High-order outflow boundary conditions [57] were imposed at the outflow.

Two meshes were generated, and shown in more detail in Figures 7b and 7c. The two meshes are respectively comprised of 3094 and 6978 quadrilateral elements. The simulations were performed at polynomial orders $P = 3$ and $P = 5$, thereby carrying out 8 separate numerical experiments. The $x-y$ plane mesh was extruded in the spanwise direction z with a Fourier expansion discretised with $N_z = 64$ planes. The spanwise numerical setup was retained through all simulations. The coarse mesh yields a total number of local degrees of freedom (DoF) per variable of $3.17, 7.13M$ with $P = 3, 5$ respectively, while the fine mesh yields $7.14, 16.08M$ DoF per variable. By design, this allows for a comparison of same-DoF convergence properties (i.e. coarse mesh at $P = 5$ and fine mesh at $P = 3$). The time step employed is $\Delta t = 5 \cdot 10^{-4} D/U_\infty$. In all cases analysed, time advancement of $T = 100D/U_\infty$ was ensured before collecting statistics for $T = 400D/U_\infty$, which corresponds roughly to 83 vortex shedding cycles.

Franke & Frank [58] discussed the importance of the time averaging window, presenting results collected over $T = 200D/U_\infty$ but highlighting that average statistics in the wake would require a longer integration window. Parnaudeau et al. [59] later showed that the recirculation length L_r requires over 250 shedding cycles to converge, and estimated that time averaging over 52 vortex shedding cycles leads to an uncertainty of roughly 10% in the prediction of the peak of fluctuating velocity components. Therefore, caution must be exercised when analysing results sampled with a shorter time window. For further in-depth discussion on the averaging window, the reader may refer to Lehmkuhl et al. [60] where time averages collected over 858 shedding cycles are discussed.

21
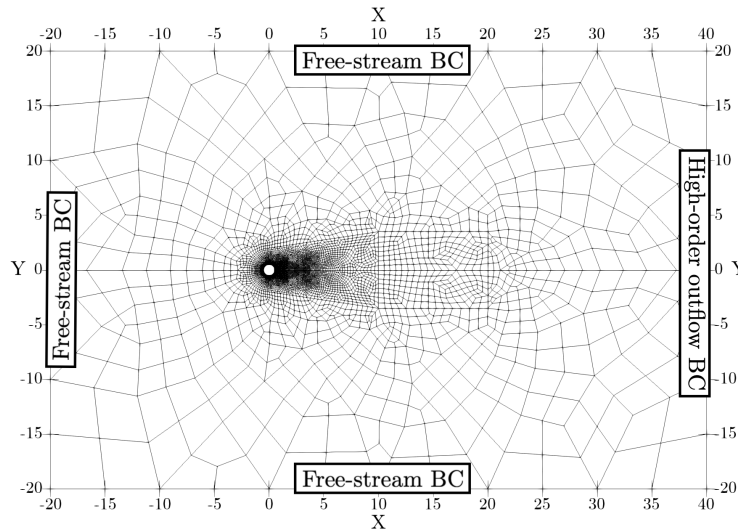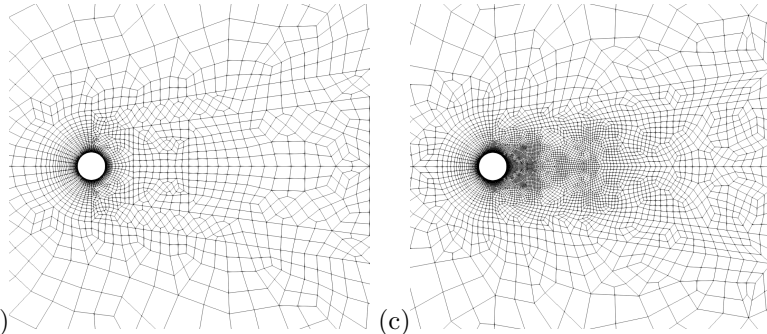
Figure 7: (a) Computational geometry and boundary conditions adopted. At the bottom, detail of the mesh in the vicinity of the cylinder: (b) coarse mesh; (c) fine mesh.

4.2.2. Results and discussion

The results presented in the figures of this section focus on the coarse mesh simulations only. Results extracted from the fine mesh demonstrate that both DGK and GJP stabilisation converge extremely closely to previous numerical and experimental measurements, but do not offer significant insight into the different accuracy levels of the two stabilisation approaches in the context of under-resolved turbulent flow simulations. As such, they are included in Appendix B for completeness but not discussed in detail in this work.

Figure 8 shows an instantaneous visualisation of the velocity magnitude calculated with the coarse mesh. The DGK formulation at $P = 3$ (top left plot) exhibits a significantly more diffusive behaviour compared with GJP (bottom left plot). As we increase P to $P = 5$ we observe the DGK formulation recovers the qualitiative features of the $P = 3$ case with GJP (comparing top right plot with bottom left

22
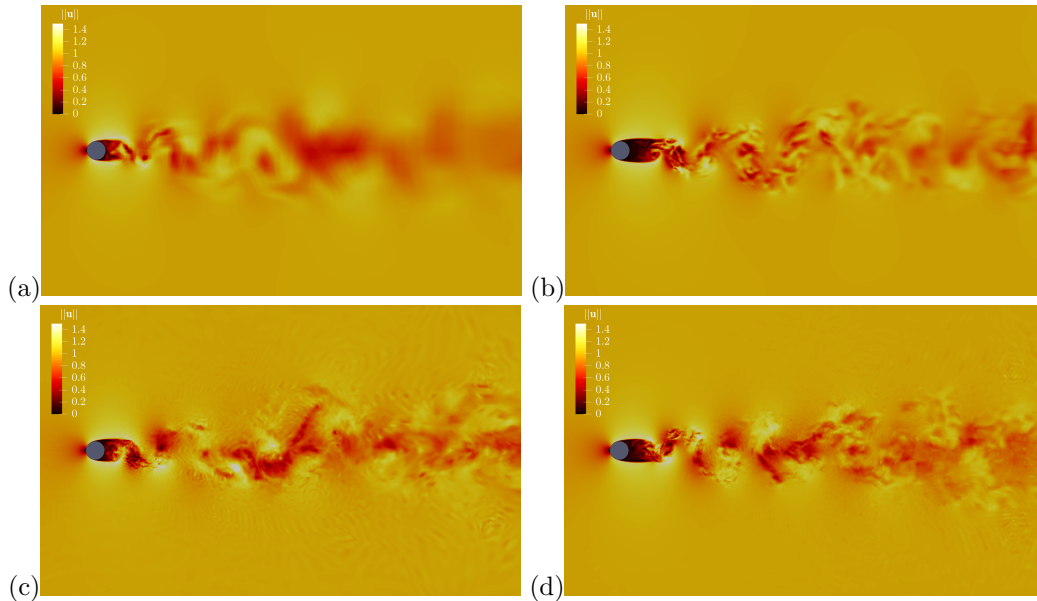
Figure 8: Instantaneous velocity magnitude extracted from a $x - y$ slice, simulated in the coarse mesh. SVV DG-Kernel is shown in the top row: (a) $P = 3$, (b) $P = 5$. GJP stabilisation is shown in the bottom row: (c) $P = 3$, (d) $P = 5$.

plot). However the $P = 5$ DGK case still exhibits a more dissipative behaviour in the coarsening region of the far wake when compared to the $P = 5$ GJP simulation (bottom right plot).

As discussed previously, capturing statistical flow features for this problem requires long averaging times [59], and large discrepancies are reported in the literature [60]. Table 1 reports the values of various statistical measurements, i.e. drag coefficient C_d, the recirculation length L_r/D and separation angle θ_{sep} for both meshes and polynomial orders and the two stabilisation approaches.

First, considering the drag coefficient we note that while both DGK and GJP converge to $C_d \approx 0.98$ on the fine mesh at $P = 5$, C_d in all GJP cases remains within 2% of the reference value, while for DGK the relative error of the fine mesh at $P = 3$ is 5.74%. This highlights the superior accuracy of the GJP approach at low resolution and especially at low polynomial order, where the dissipative behaviour of DGK hinders its accuracy in capturing statistical quantities. A similar observation can be made for the recirculation lengths L_r/D where we observe that GJP yields consistent values in the two cases at $P = 5$, and reasonable agreement is also obtained comparing DGK and GJP at the finest resolution. Finally, the separation angle is measured as $\theta_{\text{sep}} \approx 86.6$ in both cases. This property is captured consistently at all resolution levels with GJP, while DGK at $P = 3$ notably overestimates the extent of the attached flow region. We do however observe that for the DGK method better accuracy is achieved via p-refinement over h-refinement for the similar level of degrees of freedom.

The relative resolution properties of the two stabilisation techniques and the role of p-refinement on the coarse mesh is also highlighted in Figure 9, which shows the time and span-wise averaged pressure

23

Table 1: Quantitative comparison of time-averaged flow properties, compared with reference experimental and numerical studies.

	C_d		L_r/D		θ_{sep} [°]	
	DGK	GJP	DGK	GJP	DGK	GJP
Coarse, P=3	1.00719	0.999278	1.20879	1.39854	94.85	86.83
Coarse, P=5	0.933542	0.977452	1.84479	1.53705	85.97	86.56
Fine, P=3	0.926216	0.99081	1.76641	1.45229	89.76	86.72
Fine, P=5	0.982638	0.980388	1.50396	1.54253	86.59	86.59
Witherden et al. [61]	-		-		86.90	
Parnaudeau et al. [59]	-		1.51		-	
Franke et al. [58]	0.978		1.64		88.2	
Lehmkuhl et al. [60]	1.015		1.36		88	

coefficient distribution around the cylinder. The pressure distribution of DGK at $P = 3$ reveals pressure oscillations which are typically a symptom of under-resolution. A polynomial order increase to $P = 5$ improves on this aspect, but a discrepancy in the prediction of the pressure recovery in the separated region can still be observed. On the other hand, all pressure distributions obtained via GJP are overlapped with one another, as well as reference numerical data from Witherden et al. [61].

Finally we consider the velocity wake measurements. Figure 10 shows the horizontal velocity along the centre line, comparing the coarse mesh simulations with a number of previously reported numerical [61] and experimental [62, 63, 59] studies. A significant scatter exists among experimental measurements. Partly, the difference in location of the minimum recirculating velocity is justified by the slightly different Reynolds number measured by Norberg [63]. Additionally, Kravchenko and Moin [64] attributed the differences between LES computations and experiments to the presence of background turbulence in the experiments, leading to a reduced recirculation region. The differences between the various experimental data highlights the sensitivity of the wake measurements to incoming flow conditions.

The *Nektar++* simulation with GJP at $P = 3$ correctly captures the wake trend, slightly underestimating the extent of the recirculation region; $P = 5$ provides an extremely close prediction to the experiments of Parneadeu et al. [59] and numerical calculations of Witherden et al. [61]. However, the SVV approach struggles to accurately predict the velocity evolution: at $P = 3$ the recirculation region is significantly under-predicted, and over-predicted at $P = 5$. We note that the GJP and DGK predictions on the fine mesh at $P = 5$ were coincident with previous experimental and numerical results.

Time-averaged wake traverses of horizontal and vertical velocity on the coarse mesh are shown in Figure 11. Poorly resolved simulations are characterised by a "v-shaped" streamwise velocity profile, owing to early shear layer transition which promotes the penetration of velocity fluctuations in the
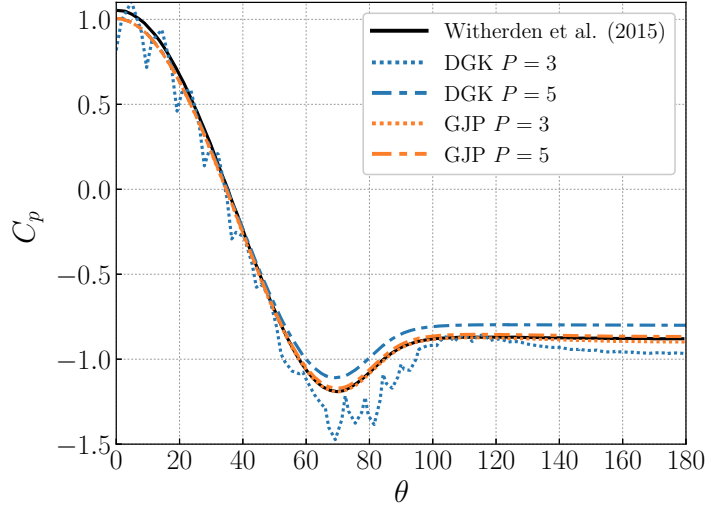
Figure 9: Time- and spanwise-averaged pressure coefficient, comparing SVV and GJP at $P = 3, 5$ on the coarse mesh, and reference numerical results of Witherden et al. [61]
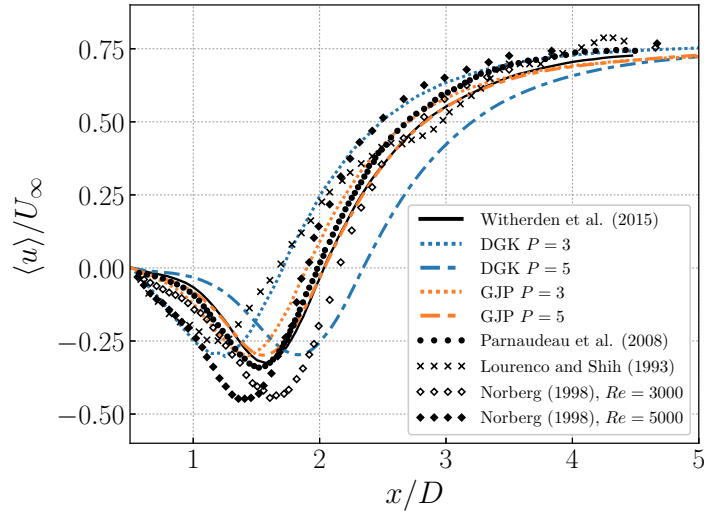

Figure 10: Time- and spanwise-averaged streamwise velocity wake profile along the centre line, compared with numerical results of Witherden et al. [61] and various experimental results. Results computed on the coarse mesh.

region immediately behind the cylinder. This can be appreciated in the DGK simulation performed on the coarse mesh at $P = 3$, measured at $x/D = 1.06$. The SVV approach with DG-Kernel does not accurately represent the near-wake behaviour in the coarse mesh, while the GJP approach at $P = 3$ manifests minor discrepancies when compared against previous studies [61, 59] and the more refined simulations. Therefore GJP stabilisation showcases excellent agreement with the reference data at all wake traverse locations for both $P = 3$ and $P = 5$, and such level of accuracy is only achieved on the fine
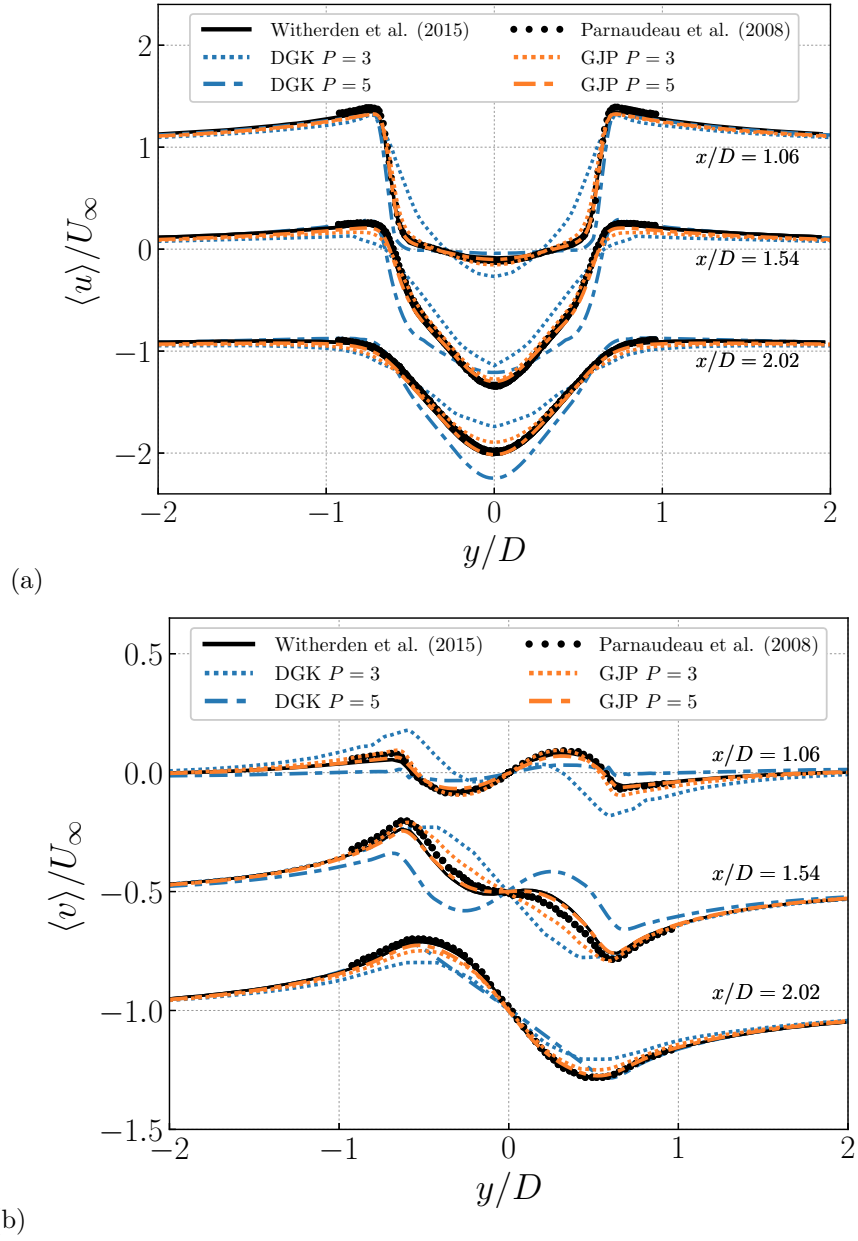
Figure 11: Time- and spanwise-averaged wake profiles of (a) horizontal velocity and (b) vertical velocity, compared with numerical results of Witherden et al. [61] and experimental results of Parneadeu et al. [59]. Results computed on the coarse mesh.

mesh at $P = 5$ with DGK. Analogous results are also observed for the fluctuating velocity components shown in Appendix B.

4.3. 3D square duct flow at $Re = 5600$

Most realistic geometries of practical interest are three-dimensional. In order to verify the effect of the two stabilisation techniques in a 3D formulation, a square duct flow is therefore considered. Indicating the half-duct width with H, the computational domain is $L_x \times L_y \times L_z = 4\pi H \times 2H \times 2H$, discretised in a hexahedral mesh with 48 spectral/hp elements in the streamwise direction x, and 38 elements in the cross-flow directions. The simulations are performed at a Reynolds number of $Re = 5600$, based on H and inflow velocity. The polynomial order is set to $P = 3$, yielding 4.436M DoF per variable and requiring a timestep of $\Delta t = 2 \cdot 10^{-4} H/U_\infty$. No-slip boundary conditions are imposed on the sidewall boundaries, and periodic conditions are adopted at the inlet and outlet. The flow is driven in the streamwise direction by imposing constant mass flux.
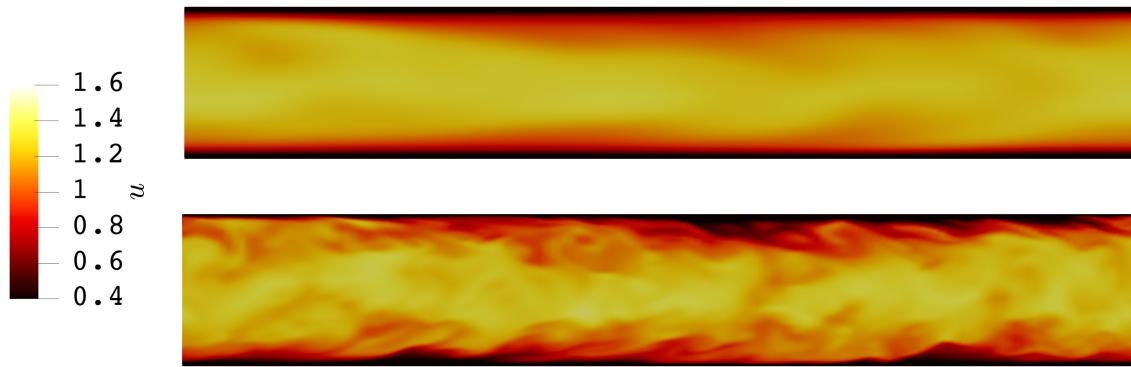
(a)

Figure 12: Instantaneous velocity magnitude extracted from a slice in the $x - y$ plane at $z/H = 0$. Top: SVV DG-Kernel; bottom: GJP stabilisation.

Statistical convergence is reached whilst stabilising the flow by means of SVV with the DG-Kernel formulation [14]. This flow solution is then used to initialise two new simulations, to compare the effect of switching to GJP stabilisation as opposed to retaining SVV stabilisation. The calculations were time-advanced by $T = 10H/U_\infty$. Figure 12 shows the velocity magnitude in a $x - y$ slice extracted at the centre of the duct. The DG-Kernel approach (shown at the top) introduces a dissipative behaviour evident through the presence of large-scale flow features only, while in the simulation relying on GJP stabilisation the flow quickly breaks down into small-scale turbulent features, within a few convective time scales. This analysis only provides qualitative insight into the different effect of the two stabilisation approaches in a fully three-dimensional spectral/hp element formulation, but highlighting that the GJP stabilisation is a promising methodology for realistic applications.

27

5. Conclusions

We have analysed the scaling and application of a Gradient Penalty Stabilisation method based on the concept of a continuous interior penalty of the jump in the gradient at the elemental boundaries of a spectral/hp element discretisation. Using an eigen-analysis of the one-dimensional advection-diffusion problem which includes the GJP stabilisation we identified an appropriate scaling of the stabilisation term that maintains a well behaved dispersion and diffusion properties. The eigenspectra of the GJP stabilised GG discretisation have analogous properties to those of a discontinous Galerkin projection which are superior at moderate polynomial orders to our previous stabilisation method using a spectral vanishing viscosity (SVV) [14]. The scaling is also consistent with previous a-priori error estimates [19]. The application of the GJP stabilisation to flow past a circular cylinder at $Re = 3900$ highlights the potential benefits of the approach in marginally resolved turbulent flows. We observe we can recover good flow characteristics at $P = 3$, whereas similar levels of accuracy require more than double the degrees of freedom with the SVV method, using $P = 5$ on a finer mesh.

References

[1] F. F. Grinstein, L. G. Margolin, W. J. Rider (Eds.), Implicit large eddy simulation, Cambridge University Press, Cambridge, 2007, computing turbulent fluid dynamics.
URL https://doi.org/10.1017/CBO9780511618604

[2] Y. Maday, E. Tadmor, Analysis of the spectral vanishing viscosity method for periodic conservation laws, SIAM J. Numer. Anal. 26 (4) (1989) 854–870.
URL https://doi.org/10.1137/0726047

[3] E. Tadmor, Shock capturing by the spectral viscosity method, Comput. Methods Appl. Mech. Engrg. 80 (1-3) (1990) 197–208, spectral and high order methods for partial differential equations

(Como, 1989).

URL https://doi.org/10.1016/0045-7825(90)90023-F

[4] E. Tadmor, Total variation and error estimates for spectral viscosity approximations, Math. Comp. 60 (201) (1993) 245–256.

URL https://doi.org/10.2307/2153164

[5] G.-S. Karamanos, G. E. Karniadakis, A spectral vanishing viscosity method for large-eddy simulations, J. Comput. Phys. 163 (1) (2000) 22–50.

URL https://doi.org/10.1006/jcph.2000.6552

[6] R. C. Moura, S. J. Sherwin, J. Peiró, Eigensolution analysis of spectral/hp continuous Galerkin approximations to advection–diffusion problems: insights into spectral vanishing viscosity, J. Comput. Phys. 307 (2016) 401–422.

URL https://doi.org/10.1016/j.jcp.2015.12.009

[7] B. Cockburn, G. E. Karniadakis, C. W. Shu, The development of discontinuous Galerkin methods, Springer, 2000.

[8] A. Ern, J.-L. Guermond, Discontinuous Galerkin methods for Friedrichs' systems. I. General theory, SIAM J. Numer. Anal. 44 (2) (2006) 753–778. doi:10.1137/050624133.

URL https://doi.org/10.1137/050624133

[9] A. Uranga, P.-O. Persson, M. Drela, J. Peraire, Implicit large eddy simulation of transition to turbulence at low Reynolds numbers using a discontinuous Galerkin method, Internat. J. Numer. Methods Engrg. 87 (1-5) (2011) 232–261.

URL https://doi.org/10.1002/nme.3036

[10] A. D. Beck, T. Bolemann, D. Flad, H. Frank, G. J. Gassner, F. Hindenlang, C.-D. Munz, High-order discontinuous Galerkin spectral element methods for transitional and turbulent flow simulations, Internat. J. Numer. Methods Fluids 76 (8) (2014) 522–548.

[11] C. Carton de Wiart, K. Hillewaert, L. Bricteux, G. Winckelmans, Implicit LES of free and wall-bounded turbulent flows based on the discontinuous Galerkin/symmetric interior penalty method, Internat. J. Numer. Methods Fluids 78 (6) (2015) 335–354.

URL https://doi.org/10.1002/fld.4021

[12] R. C. Moura, S. J. Sherwin, J. Peiró, Linear dispersion-diffusion analysis and its application to under-resolved turbulence simulations using discontinuous Galerkin spectral/hp methods, J. Comput. Phys. 298 (2015) 695–710.

URL https://doi.org/10.1016/j.jcp.2015.06.020

[13] R. C. Moura, G. Mengaldo, J. Peiró, S. J. Sherwin, On the eddy-resolving capability of high-order discontinuous Galerkin approaches to implicit LES / under-resolved DNS of Euler turbulence, J. Comput. Phys. 330 (2017) 615–623.
URL https://doi.org/10.1016/j.jcp.2016.10.056

[14] R. Moura, M. Aman, J. Peiró, S. Sherwin, Spatial eigenanalysis of spectral/hp continuous Galerkin schemes and their stabilisation via DG-mimicking spectral vanishing viscosity for high Reynolds number flows, Journal of Computational Physics (2019) 109112.

[15] J. Douglas, Jr., T. Dupont, Interior penalty procedures for elliptic and parabolic Galerkin methods (1976) 207–216. Lecture Notes in Phys., Vol. 58.

[16] E. Burman, P. Hansbo, Edge stabilization for Galerkin approximations of convection-diffusion-reaction problems, Comput. Methods Appl. Mech. Engrg. 193 (15-16) (2004) 1437–1453.
URL https://doi.org/10.1016/j.cma.2003.12.032

[17] E. Burman, M. A. Fernández, P. Hansbo, Continuous interior penalty finite element method for Oseen's equations, SIAM J. Numer. Anal. 44 (3) (2006) 1248–1274 (electronic).

[18] E. Burman, M. A. Fernández, Continuous interior penalty finite element method for the time-dependent Navier-Stokes equations: space discretization and convergence, Numer. Math. 107 (1) (2007) 39–77.
URL https://doi.org/10.1007/s00211-007-0070-5

[19] E. Burman, A. Ern, Continuous interior penalty hp-finite element methods for advection and advection-diffusion equations, Math. Comp. 76 (259) (2007) 1119–1140.
URL https://doi.org/10.1090/S0025-5718-07-01951-5

[20] E. Burman, A. Quarteroni, B. Stamm, Interior penalty continuous and discontinuous finite element approximations of hyperbolic equations, J. Sci. Comput. 43 (3) (2010) 293–312.
URL https://doi.org/10.1007/s10915-008-9232-6

[21] E. Burman, A. Quarteroni, B. Stamm, Stabilization strategies for high order methods for transport dominated problems, Boll. Unione Mat. Ital. (9) 1 (1) (2008) 57–77.

[22] M. Braack, E. Burman, V. John, G. Lube, Stabilized finite element methods for the generalized Oseen problem, Comput. Methods Appl. Mech. Engrg. 196 (4-6) (2007) 853–866.

[23] E. Burman, M. A. Fernández, Finite element methods with symmetric stabilization for the transient convection-diffusion-reaction equation, Comput. Methods Appl. Mech. Engrg. 198 (33-36) (2009)

2508–2519. `doi:10.1016/j.cma.2009.02.011`.

URL `http://dx.doi.org/10.1016/j.cma.2009.02.011`

[24] E. Burman, A. Ern, M. A. Fernández, Fractional-step methods and finite elements with symmetric stabilization for the transient Oseen problem, ESAIM Math. Model. Numer. Anal. 51 (2) (2017) 487–507.

URL `https://doi.org/10.1051/m2an/2016028`

[25] E. Burman, Interior penalty variational multiscale method for the incompressible Navier-Stokes equation: monitoring artificial dissipation, Comput. Methods Appl. Mech. Engrg. 196 (41-44) (2007) 4045–4058.

URL `https://doi.org/10.1016/j.cma.2007.03.025`

[26] E. Burman, Robust error estimates for stabilized finite element approximations of the two dimensional Navier-Stokes' equations at high Reynolds number, Comput. Methods Appl. Mech. Engrg. 288 (2015) 2–23.

URL `https://doi.org/10.1016/j.cma.2014.11.006`

[27] P. W. Schroeder, G. Lube, Pressure-robust analysis of divergence-free and conforming FEM for evolutionary incompressible Navier-Stokes flows, J. Numer. Math. 25 (4) (2017) 249–276. `doi:10.1515/jnma-2016-1101`.

URL `https://doi.org/10.1515/jnma-2016-1101`

[28] P. W. Schroeder, G. Lube, Divergence-free $H(\text{div})$-FEM for time-dependent incompressible flows with applications to high Reynolds number vortex dynamics, J. Sci. Comput. 75 (2) (2018) 830–858. `doi:10.1007/s10915-017-0561-1`.

URL `https://doi.org/10.1007/s10915-017-0561-1`

[29] E. Burman, A. Ern, Continuous interior penalty hp-finite element methods for advection and advection-diffusion equations, Math. Comp. 76 (259) (2007) 1119–1140 (electronic).

[30] R. Codina, Stabilized finite element approximation of transient incompressible flows using orthogonal subscales, Comput. Methods Appl. Mech. Engrg. 191 (39-40) (2002) 4295–4321.

[31] E. Burman, M. A. Fernández, Galerkin finite element methods with symmetric pressure stabilization for the transient Stokes equations: stability and convergence analysis, SIAM J. Numer. Anal. 47 (1) (2008/09) 409–439. `doi:10.1137/070707403`.

URL `http://dx.doi.org/10.1137/070707403`

[32] R. Codina, Stabilization of incompressibility and convection through orthogonal sub-scales in finite element methods, Comput. Methods Appl. Mech. Engrg. 190 (13-14) (2000) 1579–1599.

[33] T. Warburton, J. S. Hesthaven, On the constants in hp-finite element trace inverse inequalities, Comput. Methods Appl. Mech. Engrg. 192 (25) (2003) 2765–2773. `doi:10.1016/S0045-7825(03)00294-9`.
URL `https://doi.org/10.1016/S0045-7825(03)00294-9`

[34] E. Burman, J. Guzman, Implicit-explicit multistep formulations for finite element discretisations using continuous interior penalty, arXiv e-prints (2020) `arXiv:2012.05727arXiv:2012.05727`.

[35] E. Burman, M. A. Fernández, Continuous interior penalty finite element method for the time-dependent Navier–Stokes equations: space discretization and convergence, Numerische Mathematik 107 (1) (2007) 39–77.

[36] E. Burman, Interior penalty variational multiscale method for the incompressible Navier–Stokes equation: Monitoring artificial dissipation, Computer Methods in Applied Mechanics and Engineering 196 (41-44) (2007) 4045–4058.

[37] E. Burman, M. A. Fernández, Finite element methods with symmetric stabilization for the transient convection–diffusion–reaction equation, Computer Methods in Applied Mechanics and Engineering 198 (33-36) (2009) 2508–2519.

[38] E. Burman, Robust error estimates for stabilized finite element approximations of the two dimensional Navier–Stokes' equations at high Reynolds number, Computer Methods in Applied Mechanics and Engineering 288 (2015) 2–23.

[39] R. C. Moura, S. J. Sherwin, J. Peiró, Eigensolution analysis of spectral/hp continuous Galerkin approximations to advection-diffusion problems: insights into spectral vanishing viscosity, Journal of Computational Physics 307 (2016) 401–422.

[40] G. E. Karniadakis, S. J. Sherwin, Spectral/hp element methods for computational fluid dynamics, 2nd Edition, Oxford University Press, 2005.

[41] G. Mengaldo, R. C. Moura, B. Giralda, J. Peiró, S. J. Sherwin, Spatial eigensolution analysis of discontinuous Galerkin schemes with practical insights for under-resolved computations and implicit LES, Computers & Fluids 169 (2018) 349–364.

[42] R. C. Moura, S. J. Sherwin, J. Peiró, Linear dispersion-diffusion analysis and its application to under-resolved turbulence simulations using discontinuous Galerkin spectral/hp methods, Journal of Computational Physics 298 (2015) 695–710.

[43] G. Mengaldo, D. De Grazia, R. C. Moura, S. J. Sherwin, Spatial eigensolution analysis of energy-stable flux reconstruction schemes and influence of the numerical flux on accuracy and robustness, Journal of Computational Physics 358 (2018) 1–20.

[44] P. Fernandez, R. C. Moura, G. Mengaldo, J. Peraire, Non-modal analysis of spectral element methods: Towards accurate and robust large-eddy simulations, Computer Methods in Applied Mechanics and Engineering 346 (2019) 43–62.

[45] R. C. Moura, P. Fernandez, G. Mengaldo, S. J. Sherwin, Temporal eigenanalysis of HDG methods for linear advection-diffusion, Research report, Instituto Tecnológico de Aeronáutica (2018).

[46] F. Q. Hu, H. L. Atkins, Eigensolution analysis of the discontinuous Galerkin method with nonuniform grids: I. one space dimension, Journal of Computational Physics 182 (2) (2002) 516–545.

[47] R. C. Moura, G. Mengaldo, J. Peiró, S. J. Sherwin, On the eddy-resolving capability of high-order discontinuous Galerkin approaches to implicit LES / under-resolved DNS of Euler turbulence, Journal of Computational Physics 330 (2017) 615–623.

[48] C. H. K. Williamson, Vortex Dynamics in the Cylinder Wake, Annu. Rev. Fluid. Mech 28 (1996) 477–539. `doi:10.1146/annurev.fl.28.010196.002401`.

[49] A. Cassinelli, F. Montomoli, P. Adami, S. J. Sherwin, High Fidelity Spectral/hp Element Methods for Turbomachinery, in: Proceedings of the ASME Turbo Expo, Oslo, Norway, 2018, pp. GT2018–75733. `doi:10.1115/GT2018-75733`.

[50] G. Mengaldo, D. Moxey, M. Turner, R. C. Moura, A. Jassim, M. Taylor, J. Peiró, S. J. Sherwin, Industry-relevant implicit large-eddy simulation of a high-performance road car via spectral/hp element methods (2020). `arXiv:2009.10178`.

[51] D. Moxey, C. D. Cantwell, Y. Bao, A. Cassinelli, G. Castiglioni, S. Chun, E. Juda, E. Kazemi, K. Lackhove, J. Marcon, G. Mengaldo, D. Serson, M. Turner, H. Xu, J. Peiró, R. M. Kirby, S. J. Sherwin, Nektar++: Enhancing the capability and application of high-fidelity spectral/hp element methods, Computer Physics Communications 249 (2019) 107110. `doi:10.1016/j.cpc.2019.107110`.

[52] G. E. Karniadakis, M. Israeli, S. A. Orszag, High-order splitting methods for the incompressible Navier-Stokes equations, Journal of Computational Physics 97 (2) (1991) 414–443. `doi:10.1016/0021-9991(91)90007-8`.

[53] J. L. Guermond, J. Shen, Velocity-Correction Projection Methods for Incompressible Flows, SIAM Journal on Numerical Analysis 41 (1) (2003) 112–134. `doi:10.1137/S0036142901395400`.

[54] G. Mengaldo, D. De Grazia, D. Moxey, P. E. Vincent, S. J. Sherwin, Dealiasing techniques for high-order spectral element methods on regular and irregular grids, Journal of Computational Physics 299 (2015) 56–81.

[55] G. E. Karniadakis, S. J. Sherwin, Spectral/hp Element Methods for Computational Fluid Dynamics, 2nd Edition, Oxford University Press, Oxford, 2005.

[56] Y. Maday, S. M. O. Kaber, E. Tadmor, Legendre pseudospectral viscosity method for nonlinear conservation laws, SIAM Journal on Numerical Analysis 30 (2) (1993) 321–342.

[57] S. Dong, G. E. Karniadakis, C. Chryssostomidis, A robust and accurate outflow boundary condition for incompressible flow simulations on severely-truncated unbounded domains, Journal of Computational Physics 261 (2014) 83–105. `doi:10.1016/j.jcp.2013.12.042`.

[58] J. Franke, W. Frank, Large eddy simulation of the flow past a circular cylinder at Re=3900, Journal of Wind Engineering and Industrial Aerodynamics 90 (2002) 1191–1206. `doi:10.1016/S0167-6105(02)00232-5`.

[59] P. Parnaudeau, J. Carlier, D. Heitz, E. Lamballais, Experimental and numerical studies of the flow over a circular cylinder at Reynolds number 3900, Physics of Fluids 20 (8) (2008). `doi:10.1063/1.2957018`.

[60] O. Lehmkuhl, I. Rodríguez, R. Borrell, A. Oliva, Low-frequency unsteadiness in the vortex formation region of a circular cylinder, Physics of Fluids 25 (8) (2013). `doi:10.1063/1.4818641`.

[61] F. D. Witherden, B. C. Vermeire, P. E. Vincent, Heterogeneous computing on mixed unstructured grids with PyFR, Computers and Fluids 120 (2015) 173–186. `doi:10.1016/j.compfluid.2015.07.016`.

[62] L. M. Lourenco, C. Shih, Characteristics of the plane turbulent near wake of a circular cylinder, a particle image velocimetry study (1993).

[63] C. Norberg, LDV-measurements in the near wake of a circular cylinder, in: Advances in understanding of bluff body wakes and vortex-induced vibration, no. June, Washington, D.C., USA, 1998, pp. 1–12.

[64] A. G. Kravchenko, P. Moin, Numerical studies of flow over a circular cylinder at ReD=3900, Physics of Fluids 12 (2) (2000) 403–417. `doi:10.1063/1.870318`.

Appendix A. Eigenvalue curves

Appendix A.1. Temporal analysis eigencurves for $P = 4$ to $P = 9$

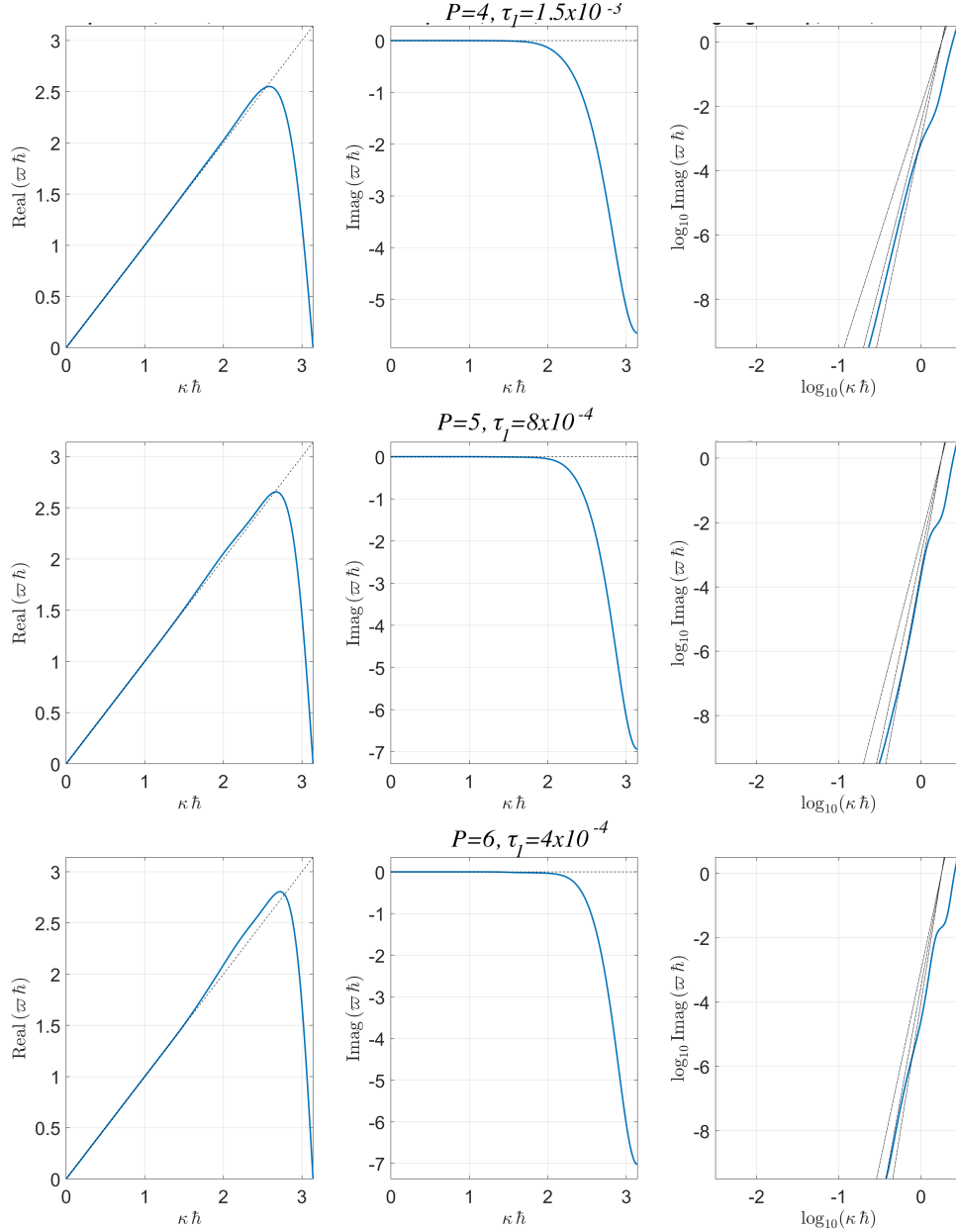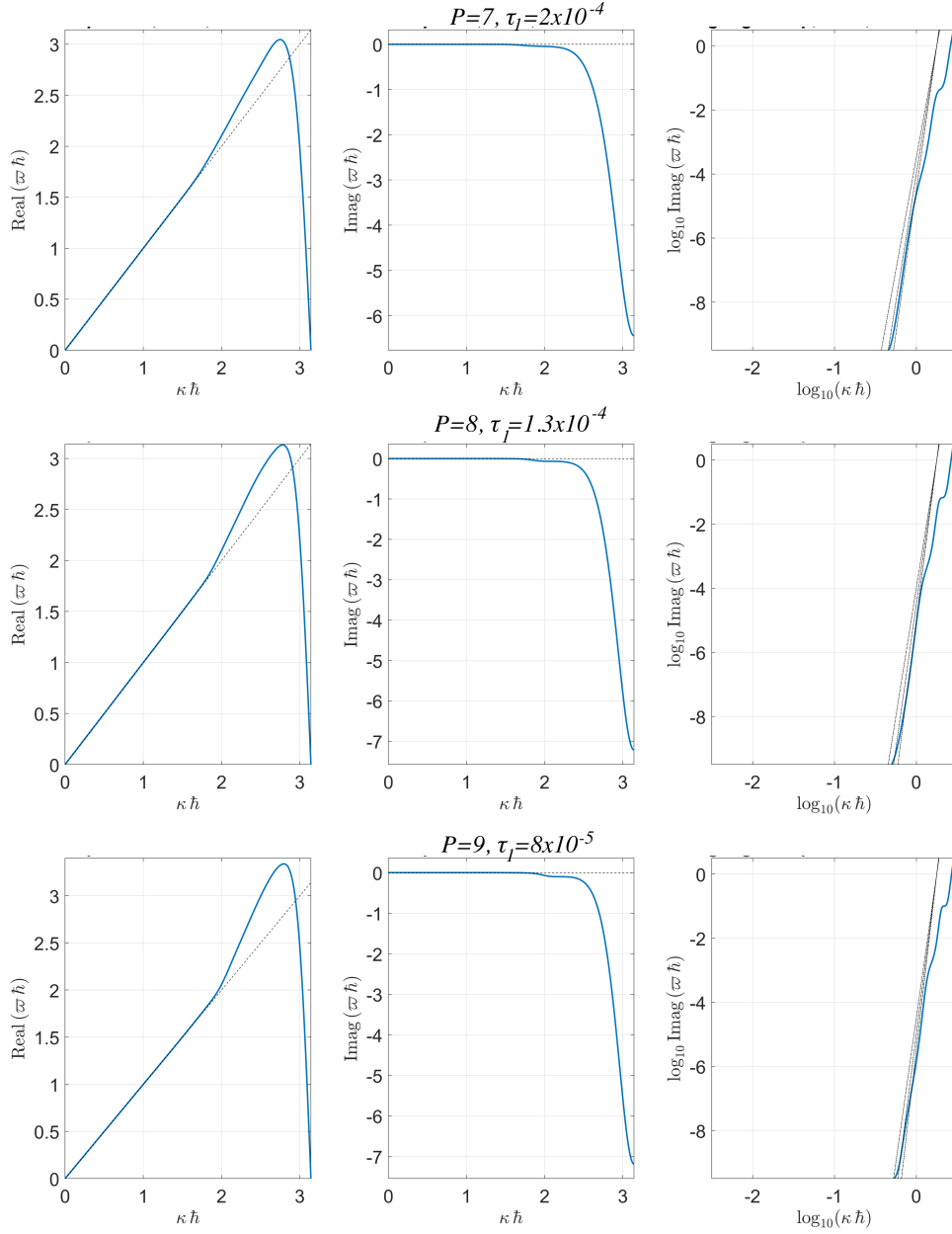Figure A.13: Numerical dispersion (left) and diffusion (middle) curves for $P = 4, \tau = 1.5^{-3}$ (top), $P = 5, \tau = 8 \times 10^{-4}$(middle) and $P = 6, \tau = 4 \times 10^{-4}$ (bottom). The diffusion curves are also shown in log-log scale on the right, where diffusion levels of (standard upwind) DG at orders $P-1$, P and $P+1$ are indicated by increasing slope as thin dash-dotted lines for reference.

Figure A.14: Numerical dispersion (left) and diffusion (middle) curves for $P = 7, \tau = 2 \times 10^{-4}$ (top), $P = 8, \tau = 1.3 \times 10^{-4}$ and $P = 9, \tau = 8 \times 10^{-5}$ (bottom). The diffusion curves are also shown in log-log scale on the right, where diffusion levels of (standard upwind) DG at orders $P - 1$, P and $P + 1$ are included as thin dash-dotted lines for reference.
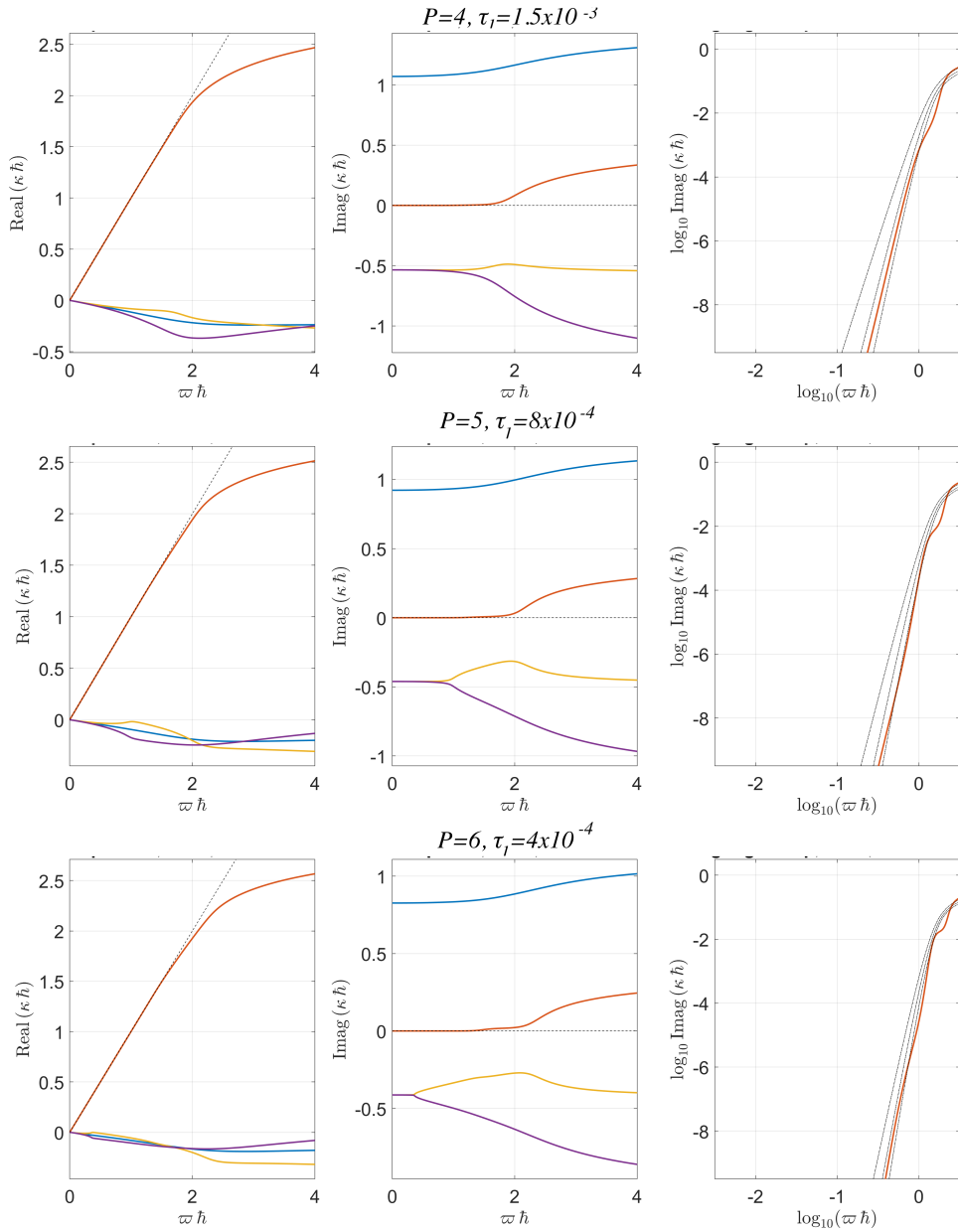
Appendix A.2. Spatial analysis eigencurves for $P = 4$ to $P = 9$

Figure A.15: Numerical dispersion (left) and diffusion (middle) curves for $P = 4, \tau = 1.5^{-3}$ (top), $P = 5, \tau = 8 \times 10^{-4}$(middle) and $P = 6, \tau = 4 \times 10^{-4}$ (bottom). The diffusion curve of the physical mode (red) is also shown in log-log scale on the right, where reference curves of (standard upwind) DG at orders $P-1$, P and $P+1$ are included as dash-dotted lines.
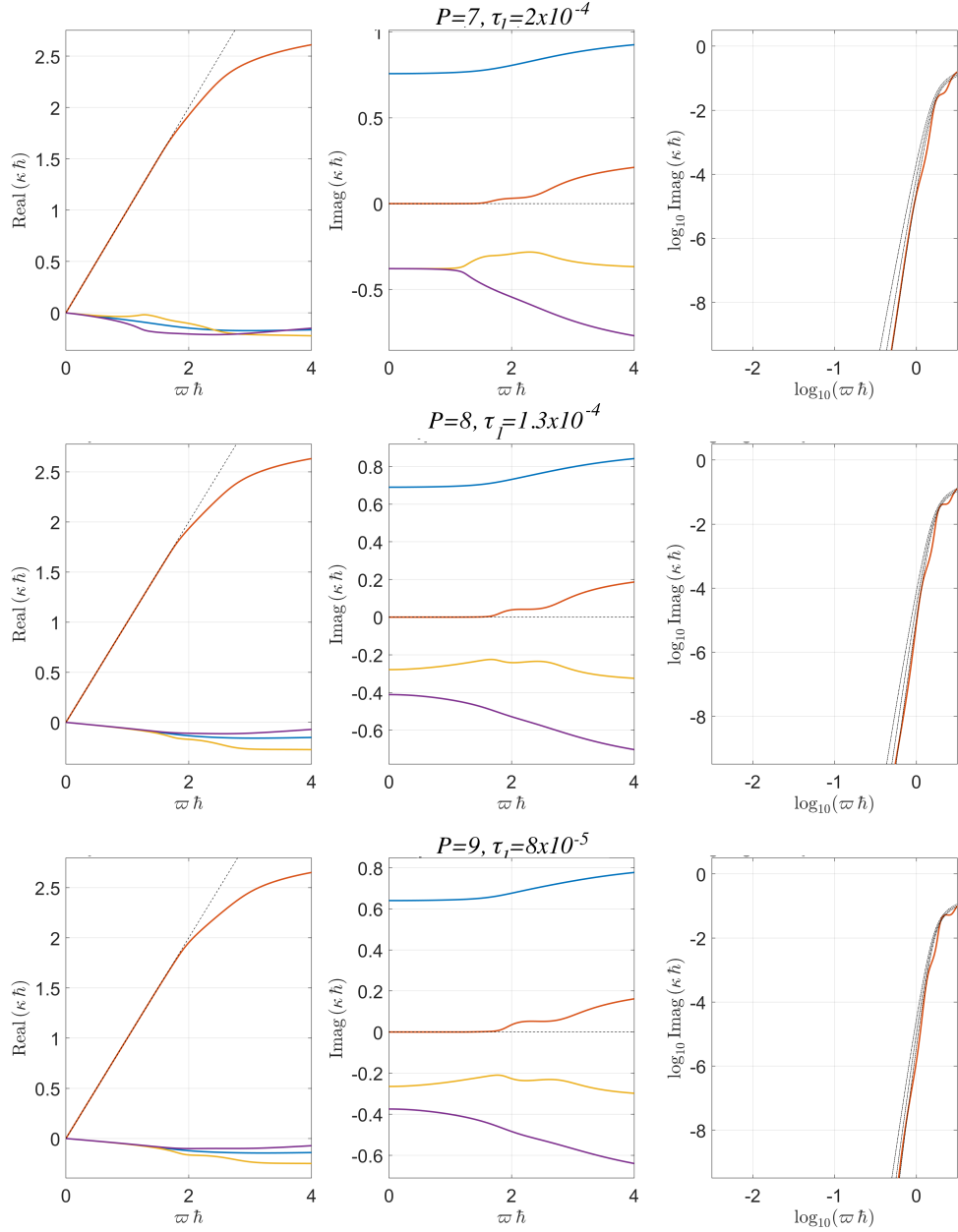
Figure A.16: Numerical dispersion (left) and diffusion (middle) curves for $P = 7, \tau = 2 \times 10^{-4}$ (top), $P = 8, \tau = 1.3 \times 10^{-4}$ and $P = 9, \tau = 8 \times 10^{-5}$ (bottom). The diffusion curve of the physical mode (red) is also shown in log-log scale on the right, where reference curves of (standard upwind) DG at orders $P - 1$, P and $P + 1$ are included as dash-dotted lines.

Appendix B. Fine mesh results and fluctuating components for flow past a cylinder at Re=3900
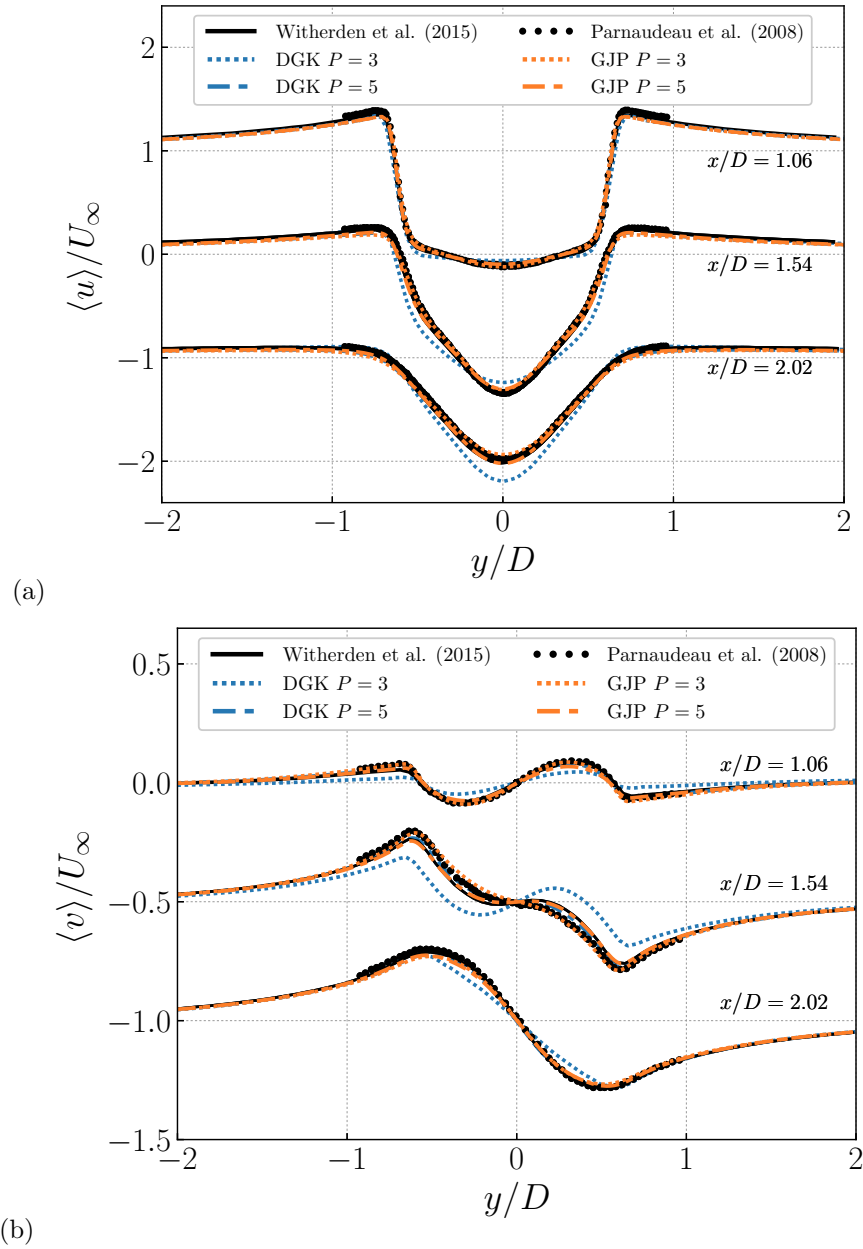

(a)

(b)

Figure B.17: Time- and spanwise-averaged wake profiles of (a) horizontal velocity and (b) vertical velocity, compared with numerical results of Witherden et al. [61] and experimental results of Parneadeu et al. [59]. Results computed on the fine mesh of Figure 7c.
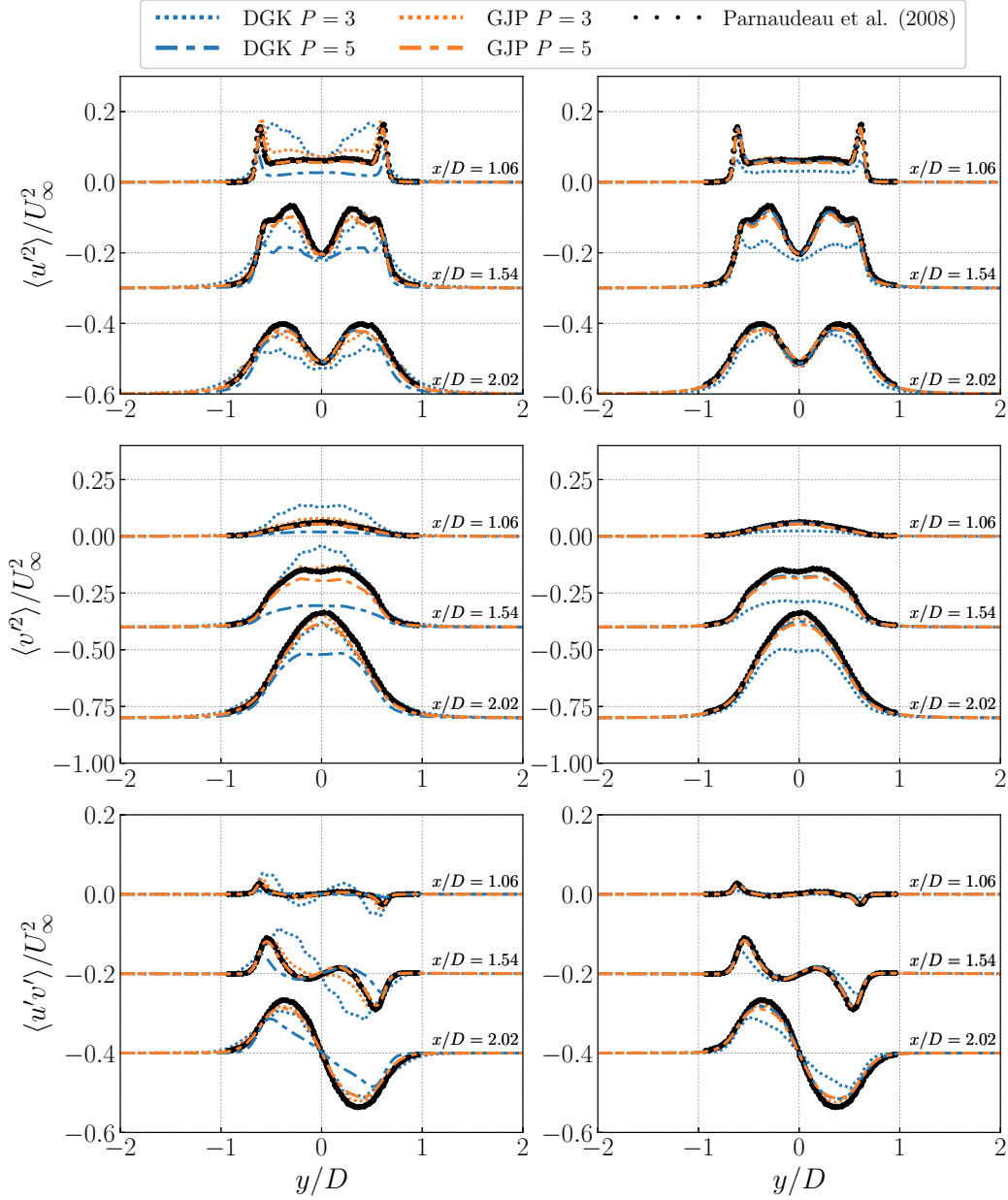
Figure B.18: Time- and spanwise-averaged fluctuating velocity profiles. Top row: $\langle u'^2 \rangle$; middle row: $\langle v'^2 \rangle$; bottom row: $\langle u'v' \rangle$. Left column: coarse mesh results (Figure 7b); right column: fine mesh results (Figure 7c). The data are compared with numerical results of Witherden et al. [61] and experimental results of Parneadeu et al. [59].